Kobe University Repository : Kernel

PDF issue: 2025-12-04

Submesoscale Coherent Structures on the Continental Shelf

Dauhajre, Daniel P.
McWilliams, James C.
Uchiyama, Yusuke

(Citation)
Journal of Physical Oceanography,47(12):2949-2976

(Issue Date)
2017-12

(Resource Type)
journal article

(Version)
Version of Record

(URL)
https://hdl.handle.net/20.500.14094/90005463

Submesoscale Coherent Structures on the Continental Shelf

DANIEL P. DAUHAJRE AND JAMES C. MCWILLIAMS

Department of Atmospheric and Oceanic Sciences, University of California, Los Angeles, Los Angeles, California

YUSUKE UCHIYAMA

Department of Civil Engineering, Kobe University, Kobe, Hyogo, Japan

(Manuscript received 8 December 2016, in final form 23 August 2017)

ABSTRACT

Discovery and analysis of submesoscale variability $O(0.3–30)$ km on the continental shelf is made possible by a high-resolution ($\Delta x = 75$ m) Regional Oceanic Modeling System (ROMS) simulation of the Southern California Bight (SCB). This variability is manifest in ubiquitous yet ephemeral coherent structures: fronts, filaments, and vortices. Similar to their open-ocean counterparts, fronts and filaments on the shelf are identified by their strong vertical velocity, surface convergence, cyclonic vorticity, and horizontal density gradient. Life cycles of these features typically last 3–5 days, with the formation dominated by a horizontal advective tendency that increases density and velocity gradients (i.e., frontogenesis). The shape of the coastline and depth of the water column both influence the abundance and spatial orientation of shallow-water fronts and filaments. Closer to shore, fronts and filaments often align themselves parallel to isobaths, and headlands often act as sites of intense vorticity generation through bottom stress. A quasi-steady, approximate momentum balance among rotation, pressure gradient, and vertical mixing—known as turbulent thermal wind (TTW)—often is valid in the strong secondary circulations local to fronts and filaments. However, front and filament circulations subject to strong diurnal variation in surface heating and vertical mixing are inconsistent with steady-state TTW balance. The secondary circulations can induce ephemeral material trapping and substantial vertical heat fluxes on the shelf.

1. Introduction

Paradigms for continental shelf dynamics have been developed from observational networks [$\Delta x \sim O(1)$ km); (Hickey et al. 2003; Cudaback and Washburn 2005; Lentz and Winant 1986; Dever 1997; Kirincich et al. 2009; Bassin and Washburn 2005; Feddersen et al. 1998], numerical simulations {Ganju et al. 2011; Romero et al. 2013; Uchiyama et al. 2014; Kumar et al. 2015, 2016; $\Delta x \sim [O(10)$ m – $O(1)$ km]}, and idealized models (Chapman 1986, 1987; Chapman and Lentz 2005; Lentz and Fewings 2012; Austin and Lentz 2002; Tilburg 2003). Recently, downscaling techniques (Mason et al. 2010) applied to coastal regions have led to numerical simulations of the shelf with horizontal resolutions of $O(10–100)$ m embedded in the regional circulation (Romero et al. 2013; Uchiyama et al. 2014; Kumar et al. 2015, 2016; Romero et al. 2016). These high-resolution simulations of coastal waters have revealed a dynamically more diverse and heterogeneous shelf than previously known, although the full variability present in these solutions remains incompletely explored. That is, there is more to shelf currents than tides, wind, internal waves, and buoyant coastal currents as well as wave-driven currents (section 2). The newly exposed shelf dynamics are primarily manifested in submesoscale coherent structures [repeatedly arising, preferred $O(0.1–10)$ km spatial patterns that are immune to swift advective deformation]: fronts, filaments, and vortices (Gula et al. 2014; Capet et al. 2008c; Mahadevan and Tandon 2006a; Nagai et al. 2006; Bracco et al. 2016; Capet et al. 2008a). These motions are a hybrid of geostrophic and ageostrophic dynamics and are defined by $O(1)$ Rossby ($\mathrm{Ro} = V/fL$) and Froude ($\mathrm{Fr} = V/NH$) numbers, where V represents a horizontal velocity;

Supplemental information related to this paper is available at the Journals Online website: https://doi.org/10.1175/JPO-D-16-0270.s1.

Corresponding author: Daniel P. Dauhajre, ddauhajre@atmos.ucla.edu

DOI: 10.1175/JPO-D-16-0270.1

© 2017 American Meteorological Society. For information regarding reuse of this content and general copyright information, consult the AMS Copyright Policy (www.ametsoc.org/PUBSReuseLicenses).

f is the Coriolis parameter; L and H are horizontal and vertical length scales, respectively; and $N = \sqrt{(-g/\rho)(\partial\rho/\partial z)}$ is the stratification, where g is the acceleration due to gravity and ρ is the density. The occurrence of these phenomena in numerical solutions is a direct consequence of increasing grid resolution to finer than $O(1)$ km (Capet et al. 2008b). Observational platforms (e.g., boats, planes, gliders) are currently incapable of adequately sampling the three-dimensional evolution of short-lived and seemingly spontaneously formed submesoscale structures over multiple-day life cycles. At present, high-resolution numerical models provide the richest realizations and the most feasible route for discovery and explanation of submesoscale dynamics in a variety of oceanographic settings.

Analysis and interpretation of submesoscale currents (reviewed in section 3) has primarily been approached in an open-ocean context where submesoscale currents most commonly reside in the surface boundary layer of relatively deep-water columns $O(100–5000)$ m. Some evidence of submesoscale phenomena in the nearshore waters on the shelf is the subject of previous work. DiGiacomo and Holt (2001), Bassin and Washburn (2005), and Kirincich (2016) provide observational evidence of submesoscale eddies in the Southern California Bight (SCB) and Martha's Vineyard shelf, respectively. Romero et al. (2013), Uchiyama et al. (2014), and Romero et al. (2016) show the occurrence of submesoscale activity on the SCB shelf through numerical simulations, and Capet et al. (2008a) does so for the Argentinian shelf. These modeling studies are primarily concerned with metrics of material lateral dispersion.

This study investigates the phenomenology of submesoscale variability on the continental shelf with a numerical simulation of the SCB with a resolution of $\Delta x = 75$ m (section 4) that resolves coastal ocean physics deep within the submesoscale range. The numerical realization motivates the following questions: 1) Do submesoscale currents exist on the shelf? 2) What are the similarities and differences between open-ocean and shelf submesoscale dynamics? 3) How does the coastal submesoscale regime phenomenologically compare with other shelf dynamics? The existence of submesoscale currents on the shelf is not necessarily surprising given the numerous, recent studies uncovering processes that drive submesoscale motions (ambient lateral buoyancy gradients, surface mixed layers, and mesoscale straining flows), which exist in some form on the shelf. Thus, a portion of the analysis is analogous to previous work relative to the offshore submesoscale regime (e.g., Gula et al. 2014) that investigates formation mechanisms and dynamical balances of cold filaments as well as the ability of individual submesoscale structures to laterally organize dissolved materials. In addition, however, we analyze the unique features of coastal submesoscale variability: how do the shape of the coastline, vertically overlapping boundary layers, and contact of flow with the bottom influence the distribution, formation, local circulation, and evolution of submesoscale structures on the shelf? Furthermore, we contextualize certain aspects of submesoscale phenomenology with other shelf currents: for example, how do the vertical heat fluxes induced by an individual submesoscale front or filament compare with vertical heat fluxes caused by an internal wave? How do the density gradients on the shelf associated with submesoscale currents differ from density gradients caused by shelfbreak or tidal mixing fronts? Because submesoscale currents preferentially are manifested in coherent structures, much of the analysis focuses on isolated structures (a single front, filament, or vortex). We supplement the analysis of individual submesoscale structures with statistical metrics to contextualize and strengthen interpretations.

This study is an intersection of two scientific communities: shelf circulation and submesoscale variability (reviewed in sections 2 and 3, respectively). The purpose of the study is twofold: to introduce submesoscale variability to the coastal community and to investigate the degree of control by unique aspects of the shelf (e.g., its shallow depth) on submesoscale currents not previously explored in open-ocean studies (Gula et al. 2014; Capet et al. 2008b; Shcherbina et al. 2013). Our goals are to provide evidence for and to characterize the shallow-water submesoscale regime and highlight its potential importance in contributing horizontal and vertical material fluxes near the coast in the context of the more familiar dynamics of open-ocean submesoscale currents and other types of currents on the continental shelf.

2. Background: Types of shelf circulation

To provide context for submesoscale processes on the shelf, we give an overview of the common dynamical paradigms for shelf circulation. We restrict our attention to paradigms relevant to the Regional Oceanic Modeling System (ROMS) solutions for the SCB (section 4); these solutions contain no surface gravity waves and lack significant freshwater input from the shoreline.

a. Coastal geography: Defining the shelf partitions

Before we overview the types of shelf circulation germane to the SCB shelf, we present a cross-shore partitioning of the coastal ocean to define terms, partly because the terminology varies in previous literature. Our partition of the coastal ocean regions along a cross-shore axis is in Fig. 1 and its caption. We highlight two regions in Fig. 1: the surf–shelf transition zone (SSTZ) and the continental shelf. The SSTZ (commonly referred to as

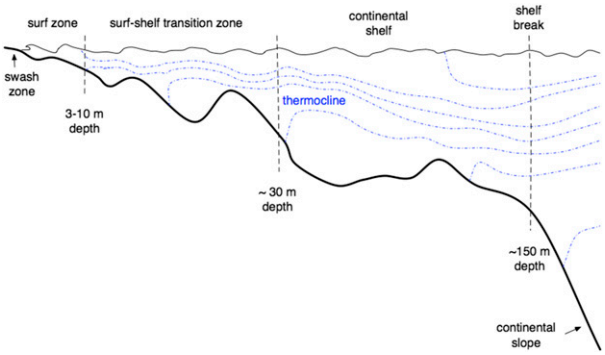

FIG. 1. An illustration of the cross-shore partitioning of the stratified coastal ocean: surface waves break and drive littoral currents in the surfzone that extends seaward to the edge of the SSTZ. The SSTZ is characterized by overlapping surface and bottom boundary layers and extends to the offshore point where surface and bottom boundary layers separate (continental shelf). The continental shelf has surface and bottom boundary layers separated by a stratified interior and extends to the shelf break. Strong along-slope currents and mesoscale variability are common on the continental slope.

the inner-shelf[1]) is defined as the region seaward of the surfzone where surface and bottom boundary layers (SBL and BBL) overlap. The continental shelf intersects the SSTZ where SBL and BBL separate, inshore of the shelf break and continental slope. This study describes submesoscale variability mainly inshore of the shelf break; boundary layer overlap is thus spatiotemporally variable in the domain of interest.

b. Tidal circulation

The interaction of tidal flows with nonuniform topography can generate residual tidal flow patterns (e.g., tidal eddies) that are quasi-permanent dynamical features on a shelf (Maddock and Pingree 1978; Robinson 1981; Geyer and Signell 1990; Ganju et al. 2011). We note the presence of such tidal eddies in our simulations (briefly discussed in section 5a relative to Fig. 4); however, analysis of their dynamics is not necessarily pertinent to this study. Buijsman et al. (2012) investigate the internal tide (section 2d) variability of the SCB with a similar ROMS simulation.

Tides can also be responsible for setting up long-lived lateral density gradients on the shelf, known as tidal mixing fronts (Simpson and Hunter 1974; Loder et al. 1993; Hill et al. 1993). These fronts represent a persistent transition zone from vertically mixed to stratified waters on the shelf and result from a competition between vertical mixing induced by the tide and stratification induced by surface heat flux (Simpson and Hunter 1974) or river discharge. They have been observed, for example, on the northwest European shelf (Simpson and Hunter 1974; Simpson 1981) and more recently in the Middle Atlantic Bight (Loder et al. 1993; Dale et al. 2003; Ullman et al. 2003; Chen et al. 2003). The density gradients associated with these fronts have alongshore geostrophic jets as well as cross-shore secondary circulations across the density gradient that exhibit surface convergence along the geostrophic jet (Chen et al. 2003).

c. Wind-driven circulation

Taking the viewpoint of a relatively unstratified shelf, depth-averaged momentum balances (Lentz and Winant 1986; Lentz and Fewings 2012; Feddersen et al. 1998) are frequently used to interpret along-shelf variability. A common yet simple reduction of the alongshore, depth-averaged momentum balance assumes a balance among acceleration, the alongshore pressure gradient, and surface and bottom stresses (Lentz and Fewings 2012); this reduced momentum balance has been used to describe alongshore current variability in the SCB (Lentz and Winant 1986; Hickey et al. 2003; Kumar et al. 2015). Hickey et al. (2003) in an analysis of an observational network in the SCB draw the conclusion that wind stress (local or remote) drives half of the subtidal velocity variance on the SCB shelf with local winds driving more variance in the spring than summer. Remote wind forcing is primarily thought to locally manifest as poleward-propagating coastal trapped waves (CTWs; Chapman 1987; Kim et al. 2013).

The vertical structure of shelf flows (along and cross shelf) has mainly been understood through wind-forced models (Lentz and Chapman 2004; Tilburg 2003; Austin and Lentz 2002; Federiuk and Allen 1996) with stratification playing a large role in dictating the dynamics. Cross-shelf flow is primarily viewed as a two-layer structure with an onshore (offshore) flow at the surface and compensating offshore(onshore) return flow in the bottom (because of the coastal boundary condition of no flow through the boundary). The wind orientation (along or cross shelf) responsible for this cross-shelf flow is dictated by the depth of the SBL (partially a function of stratification) relative to the full depth. Along-shelf winds will drive a cross-shelf Ekman flow with the cross-shore extent of the location of maximum cross-shelf convergence dictated by the stratification and wind direction (Austin and Lentz 2002; Lentz and Chapman 2004). If the SBL intersects the bottom, and surface gravity wave forcing is weak, cross-shelf winds can drive cross-shelf flow (Tilburg 2003; Lentz and Fewings 2012; Cudaback and Washburn 2005) caused by a reduction of the alongshore transport by the bottom stress with a

[1] The name inner-shelf lacks dynamical specificity; hence, we choose the name surf–shelf transition zone because it is more dynamically relevant.

cross-shelf pressure gradient forming to balance the cross-shelf wind stress.

In the SCB, diurnal band baroclinic motions ($T \in [18, 33]$ h) can be directly forced by the diurnal sea–land breeze despite being above the critical latitude (~30°) necessary for a resonant response to the diurnal wind because of modulation of the "effective" Coriolis parameter by subtidal vorticity (Federiuk and Allen 1996; Lerczak et al. 2001; Nam and Send 2013; Kumar et al. 2016). The resonant response, characterized by an upward propagation of cross-shelf flow, has been observed (Nam and Send 2013; Lerczak et al. 2001), reproduced in a linear model (Lerczak et al. 2001; Federiuk and Allen 1996), and diagnosed in ROMS (Kumar et al. 2016). We also see these motions in our ROMS solutions (section 4) but do not show them here.

d. Internal waves

The propagation of internal waves across the shelf (Lerczak et al. 2003) can be responsible for lateral cross-shelf transport (Noble et al. 2009) and substantial vertical heat flux across the pycnocline (Shroyer et al. 2010) that acts to mix the water column. From a geographical standpoint, internal wave generation sites in the SCB are mainly a function of the magnitude of the slope $|\nabla_h h|$ [Fig. 6 in Buijsman et al. (2012)] and the barotropic tide. Internal waves are seen in our ROMS solutions, specifically near the Santa Monica Bay shelf break as isotherm undulations coincident with cross-shore velocity signals emanating from the shelf break. However, because of the hydrostatic approximation and limited grid resolution, the nearshore ROMS solutions do not contain a full realization of the internal wave regime, specifically with respect to bore formation and wave breaking.

e. Shelfbreak fronts

Analogous to submesoscale fronts and filaments, shelfbreak fronts are characterized by large horizontal density gradients. However, unlike the ephemeral submesoscale shallow-water fronts and filaments shown in this study, shelfbreak fronts exist on long time scales (seasonal/yearly), despite being subject to external perturbations (Chapman 2000). These cross-shore density gradients are generally thought to form and exist over gently sloped continental shelves. They have mainly been studied on the Middle Atlantic Bight shelf (Chapman and Beardsley 1989; Linder and Gawarkiewicz 1998; Chen and He 2010) but are known to exist on other shelves in east Greenland, the east Bering Sea, and the Celtic Sea (Zhang and Gawarkiewicz 2015) and are not expected to be prevalent on the steep SCB shelf.

Chapman and Lentz (1994; and later Chapman 2000) suggest a "frontal trapping" mechanism to explain the formation and maintenance of shelfbreak fronts. An alongshore, coastal current generates offshore transport in the BBL that leads to the formation of a full-depth density gradient caused by advection of the fresher water offshore. The front becomes trapped at the depth where the near-bottom geostrophic along-shelf flow changes sign with the result that the BBL Ekman transport converges.[2]

f. Ephemeral submesoscale currents

The submesoscale shelf fronts and filaments analyzed in the remainder of this paper are ephemeral (i.e., with life cycles that span several days), are characterized by very high Rossby number Ro (equal to the peak vertical vorticity ζ divided by the Coriolis frequency f), and can be created by ambient mesoscale straining flows and/or interaction with the coastline. In this regard, they represent a different type of lateral density gradient on the shelf relative to the spatially confined, long-lived, lower Ro shelfbreak and tidal mixing fronts discussed above. Further, they are consistently straddling the intersection of the SSTZ and continental shelf (i.e., the transverse axis of the features spans regions of boundary layer overlap and boundary layer separation) and often extend even farther into deep water. Strong vertical mixing is central to their maintenance and gives rise to substantial vertical structure in their circulation. The local circulation associated with these structures (section 5e) does not fit any of the dynamical paradigms discussed in this section. Our view is that shallow-water submesoscale currents should be recognized as an important type of shelf variability.

3. Background: Submesoscale dynamics

The submesoscale regime (McWilliams 2016) has recently drawn much attention from the perspective of its role in the turbulent cascade of energy (Capet et al. 2008b; Barkan et al. 2015), characterization of its coherent structures (Munk et al. 2000; Mahadevan and Tandon 2006a; Nagai et al. 2006; Gula et al. 2014; McWilliams et al. 2015) and influence on density stratification in the surface layer (Boccaletti et al. 2007), and its potential ecosystem controls (Mahadevan 2016; Levy et al. 2012). Submesoscale motions fill the spectral gap between the inverse energy cascading quasigeostrophic

[2] Chapman (2000) shows that the frontal trapping depth is actually independent of the shelfbreak depth in an idealized setting. Benthuysen et al. (2015) investigate the dynamical importance of the shelf break in light of Chapman (2000) results and show that, for an upwelling front, the shelfbreak slope induces a weaker cross-shelf transport (relative to the shelf) and can move BBL convergence offshore of the shelf break.

mesoscale and forward energy cascading microscale by providing a forward route to energy dissipation through loss of balance (D'Asaro et al. 2011; Capet et al. 2008d; Barkan et al. 2015).

Submesoscale currents consistently reside in the weakly stratified SBL and have the form of "coherent structures" with preferred spatial patterns of fronts, filaments, and vortices on spatial scales of $L \sim 0.1$–10 km and $H \sim 0.01$–1 km. Previous studies (Nagai et al. 2006; Mahadevan and Tandon 2006a; Gula et al. 2014; Capet et al. 2008c) show that the individual structures (e.g., fronts and filaments) manifested on the submesoscale consist of a mixture of geostrophic and ageostrophic dynamics characterized by high Rossby number ($\mathrm{Ro} = \zeta/f \gg 1$), strong vertical velocity [$w \sim O(10^{-3})$ m s^{-1}], and large horizontal buoyancy gradients. A dynamical signature of submesoscale structures in the surface layer are lines and curves of strong, cyclonic surface vorticity [indicative of longitudinal (alongfront) geostrophic flow set up by a transverse (cross front) buoyancy gradient] and surface convergence (indicative of an ageostrophic transverse secondary circulation that produces large, downwelling vertical velocity).

Three mechanisms are commonly invoked to describe the formation of submesoscale coherent structures: generation of "mixed layer eddies" by a form of baroclinic instability in the surface mixed layer that can exhibit an unstable linear mode with a horizontal length scale of the mixed layer deformation radius $l \sim Nh_{\mathrm{SBL}}/f \sim O(1)$ km because of the weak stratification ($N \sim 10^{-3}\,\mathrm{s}^{-1}$) and shallow depth ($h_{\mathrm{SBL}} \sim 100$ m) (Boccaletti et al. 2007; Callies et al. 2016); frontogenesis (rapid sharpening of buoyancy or velocity gradients) by a favorably aligned deformation flow that elongates a buoyancy gradient by strain (Hoskins 1982; McWilliams et al. 2009a,c; Shakespeare and Taylor 2013); and frontogenesis in a turbulent boundary layer by a mixing-induced transverse secondary circulation that rapidly sharpens existing gradients by advection (McWilliams et al. 2015). A coherent structure can rapidly form, maintain its shape for hours to days while being advected by larger-scale flows fields, and ultimately be destroyed by its own instabilities (or parameterized diffusion) or by shredding from other strong flows (Gula et al. 2014; McWilliams 2016). Submesoscale fronts, filaments, and vortices are dynamically distinct ($\mathrm{Ro} \sim 1$) and relatively ephemeral [O(hours–days)] compared to geostrophically balanced ($\mathrm{Ro} \ll 1$) mesoscale eddies that often exist for O(weeks).

A steady-state approximate momentum balance combining geostrophic, Ekman, and hydrostatic dynamics has been used to diagnose and describe front and filament circulation (Gula et al. 2014; McWilliams et al. 2015; Wenegrat and McPhaden 2016). The balance, referred to as turbulent thermal wind (TTW), is applied under the assumption that the spatial configurations are quasi steady (i.e., fronts and filaments after generation and precluding destruction) and thus lacks time tendency and advection terms. The TTW balance in horizontal momentum is given by

$$f\hat{\mathbf{z}} \times \mathbf{u}_h = -\nabla_h \phi + \frac{\partial}{\partial z}\left(\kappa_v \frac{\partial \mathbf{u}_h}{\partial z}\right), \tag{1}$$

where the x axis is the longitudinal (alongfront/filament) axis and the y axis is the transverse (cross front/filament) axis. The horizontal velocity vector is $\mathbf{u}_h = u\hat{\mathbf{i}} + v\hat{\mathbf{j}}$, ϕ is the pressure (p) normalized by a reference density ($\phi = p/\rho_0$), and κ_v is the vertical eddy viscosity coefficient (usually associated with boundary layer turbulence and modeled by a vertical mixing parameterization in ROMS discussed in section 4). With hydrostatic vertical momentum balance ($\partial\phi/\partial z = -g\rho/\rho_0$), knowledge of the density structure and turbulence in the boundary layer [$\kappa_v(y, z)$] can be used to obtain a diagnostic estimate of the submesoscale coherent structure circulation by (1).

The TTW diagnostic balance when applied to ROMS solutions in Gula et al. (2014) has proven the more successful (relative to other diagnostics; Garrett and Loder 1981; Nagai et al. 2006) in diagnosing the ageostrophic secondary circulations associated with submesoscale fronts and filaments. Equation (1) gives a scaling estimate for the strength of the transverse overturning streamfunction (McWilliams 2017):

$$\Phi \sim \frac{\kappa_v \nabla_h b}{f^2}, \tag{2}$$

where the buoyancy $b = -g\rho/\rho_0$. Equation (2) states that the presence of a strong buoyancy gradient and a turbulent boundary layer are necessary to produce an ageostrophic overturning cell in the transverse plane. The neglect of an acceleration term in (1) is made with the assumption that mid–life cycle submesoscale fronts or filaments will undergo relatively slow changes in κ_v or $\nabla_h b$ and that acceleration and advection are relatively small. We investigate the validity of the TTW balance for shelf fronts and filaments in section 5e.

The strong restratification flux (Boccaletti et al. 2007) induced by submesoscale vertical velocities has been invoked as a mechanism that can aid phytoplankton growth by trapping nutrients in a newly stratified euphotic zone (Mahadevan 2016; Levy et al. 2012), and the secondary circulations can scour nutrients from below the boundary layer. Horizontal heterogeneity of submesoscale coherent structures at the surface can thus impart structure onto signals of primary productivity and partially control ecosystem functioning.

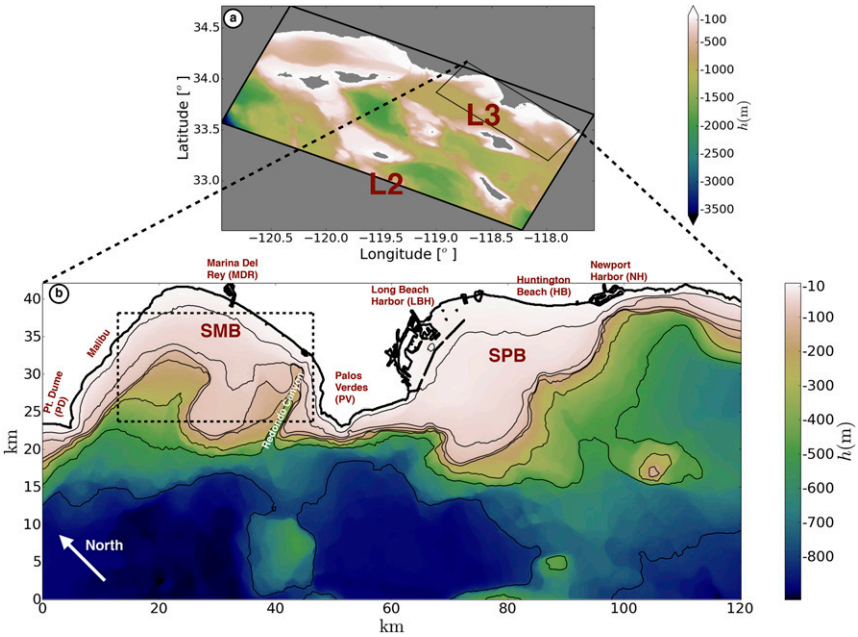

FIG. 2. (a) L2 and L3 ROMS nests with bathymetry contoured. (b) L3 domain. SMB and SPB are indicated as well as various along-coast locations to orient the reader. The dashed, black box in SMB is used for the analysis in section 5e(ii) (Fig. 12).

Finite-depth influences on submesoscale currents are unexplored because most of the literature is focused on the open-ocean regime. Submesoscale currents on the shelf are often influenced by local bathymetry. Contact with the seafloor has the potential to influence front or filament circulation because of bottom drag and vertical mixing in the BBL. The mesoscale activity contributing to the ambient straining fields commonly implicated in the formation of open-ocean submesoscale coherent structures [e.g., the deformation flow mechanism of Hoskins (1982)] may be dampened on shelves that are narrower and shallower than a typical mesoscale eddy size; however, the instability and mixing-induced frontogenesis formation mechanisms are still available there.

4. Simulation setup

The model used is ROMS (Shchepetkin and McWilliams 2005). The model solves the hydrostatic primitive equations and uses a K-profile parameterization (KPP; Large et al. 1994) for vertical mixing. The 3D circulation of Santa Monica and San Pedro Bays (SPB; Fig. 2b) is simulated with $\Delta x = 75$ m horizontal resolution. This fine resolution is achieved through a one-way grid nesting technique (Mason et al. 2010). The details of the computational time periods, grid resolution, boundary conditions, and atmospheric and tidal forcings are summarized in Table 1. The nesting hierarchy is as follows: an outer domain of $\Delta x = 5$ km (L0) for the entire U.S. West Coast, $\Delta x = 1$ km for the SCB (L1), $\Delta x = 250$ m (L2) for central area of the bight, and $\Delta x = 75$ m (L3) encompassing Santa Monica and San Pedro Bays. The L2 and L3 nests are shown in Fig. 2a, and the L3 domain is shown in Fig. 2b. The L3 nest is atmospherically forced (winds, surface heat, and freshwater fluxes) by a 6-km Weather Research and Forecast (WRF) Model (Michalakes et al. 1998) simulation within the NCEP North American Regional Reanalysis (32-km resolution). The TPXO7.1 global tidal prediction model (Egbert et al. 1994) provides the tidal amplitude and phases for 10 tidal constituents (M_2, S_2, N_2, K_2, K_1, O_1, P_1, M_f, and M_m) that are used in the forcing of the L1 solution at the side boundaries. The tidal variability in L1 is passed onto L2 through the lateral boundary condition, which serves as the boundary condition for the L3 solution. More specific details of the nesting procedure for the L3 solutions can be found in Uchiyama et al. (2014) and Romero et al. (2013).

Various regions within the L3 domain that are later referred to are labeled in Fig. 2b. Specifically, we refer to Santa Monica Bay and San Pedro Bay as SMB and SPB, respectively. The L3 hindcast spans 1 December 2007–29 April 2008. The majority of the analysis presented is based on 2-h-averaged output of the L3 solutions. There are two analyses that utilize higher-frequency output. The first is the analysis of Filament1 in section 5c based on 30-min-averaged output of L3 solutions and the second is the 15-min snapshots for offline Lagrangian particle simulations in section 5g.

TABLE 1. Configuration of ROMS nests for the SCB.

	L0	L1	L2	L3
Computational period	January 2007–December 2008	October 2007–April 2008	November 2007–April 2008	December 2007–April 2008
Horizontal resolution	5 km	1 km	250 m	75 m
Vertical levels	40	40	40	32
Boundary conditions	SODA (5 day)	L0 (daily)	L1 (2 hourly)	L2 (2 hourly)
Barotropic tide	—	TPXO7.1	—	—
Wind forcing	WRF(18 km)	WRF(6 km)	WRF(6 km)	WRF(6 km)

Numerical simulations begin to resolve submesoscale coherent structures (fronts, filaments, and vortices) with horizontal grid resolutions of about 1 km (Capet et al. 2008b; Gula et al. 2014; Romero et al. 2013; Uchiyama et al. 2014). Surface velocity data from high-frequency radar have been used to hint at the existence of submesoscale eddies on the shelf (Bassin and Washburn 2005); however, the resolution provided by the radars ($\Delta x \sim 2$ km) is not necessarily fine enough to capture the full regime (nor sample the vertical structure). High-resolution surface images [e.g., SST, color, and synthetic aperture radar (SAR)] have provided the most extensive validations of the simulated submesoscale patterns (Munk et al. 2000; DiGiacomo and Holt 2001; D'Asaro et al. 2011; McWilliams 2016).

The BBL exerts a degree of control on the shallow-water dynamics in the L3 solution. Submesoscale structures on the shelf span the full ~10–100-m water column and may be in contact with the bottom. The bottom stress in the L3 solution is computed as a bottom-layer quadratic drag law:

$$\boldsymbol{\tau}^b = \frac{\rho_0 k^2 |\mathbf{u}_b| \mathbf{u}_b}{\ln(z_b/z_0)^2}, \tag{3}$$

where $\mathbf{u}_b$ is the velocity vector of the lowest sigma level, $k = 0.41$ is von Kármán's constant, z_b is the height above the bottom (midpoint of the bottom grid cell), and z_0 is a roughness length (10^{-2} m).

The BBL thickness h_{BBL} and its associated vertical mixing in the L3 solution are parameterized with KPP. The BBL KPP scheme is analogous to the SBL scheme that determines the boundary layer depth, h_{SBL} or h_{BBL}, based on turbulent shear, stratification, and rotation (Durski et al. 2004; McWilliams et al. 2009b; Lemarie et al. 2012); the vertical mixing is then determined from the boundary layer depth, a nondimensional shape function that matches the interior mixing to vertical edges of the boundary layer, and a turbulent velocity scale (Large et al. 1994). While open questions remain on the skill KPP has relative to rapidly changing time scales [O(minutes)] and its lack of dependency on horizontal gradients, McWilliams et al. (2009b) and Durski et al. (2004) find that KPP is suitable for diurnal forcing and coastal application, respectively.

Submesoscale motions may potentially exhibit nonhydrostatic effects in the real ocean. However, our solutions are somewhat slowly evolving and scale anisotropic ($H/L \ll 1$, where H and L are vertical and horizontal length scales, respectively), and we do not expect nonhydrostatic behaviors to be important. Mahadevan and Tandon (2006b) provide a direct comparison of hydrostatic and nonhydrostatic submesoscale realizations. The study was unable to find categorical differences between the realizations, however, the comparison is made up to a resolution of $\Delta x = 250$ m. Important nonhydrostatic processes may arise at higher resolution, though this remains an open question. While nonhydrostatic effects may have some relevance in the $\Delta x = 75$ m L3 domain, the scope of our study does not include processes where nonhydrostatic effects cause the largest differences (e.g., evolution of baroclinic instability generating submesoscale features).

This study focuses on submesoscale structures that arise on or near the continental shelf of the L3 domain. The $\Delta x = 75$ m grid in the L3 solution (Fig. 2b) resolves the O(0.3–30) km spatial scales of submesoscale coherent structures as well as detailed features of the coastline that influence nearshore circulation. In Kumar et al. (2015), these L3 solutions are used as the boundary conditions for a slightly finer grid (HB06 L4 with $\Delta x = 50$ m), whose solutions are compared to mid- to inner-shelf observations off Huntington Beach. That validation study shows that the nearshore ROMS solutions well simulate subtidal dynamics on the shelf, so we do not do further model validation in this paper.

5. Submesoscale coherent structures on the shelf

A portion of the analysis in this section will focus on individual shelf fronts and filaments. We provide a summary of the names, locations, times, and relevant figures pertaining to these features in Table 2 to orient the

TABLE 2. Isolated submesoscale features analyzed in the study. Indicated in the table are the name, the type of buoyancy structure (front or filament), the general location (see Fig. 2), the date(s), time(s) (PST) of feature analysis, and the figures corresponding to each feature. For Filament1, Filament2, Filament4, and Front2, the analysis spans multiple days, so "multiple" is listed for the time(s) column, with exact hours given in the text and figures as needed.

Name	Structure	Location	Date(s)	Time(s)	Figure(s)
Filament1	Filament	SPB	31 Dec 2007–1 Jan 2008	Multiple	6
Filament2	Filament	SMB	3 Feb 2008–6 Feb 2008	Multiple	7
Filament3	Filament	SMB	14 Dec 2007	0300	8, 9
Filament4	Filament	SMB	3 Jan 2008–5 Jan 2008	Multiple	8, 11, 13
Front1	Front	SPB	21 Mar 2008	0400, 1000	8, 10
Front2	Front	SPB	13 Dec 2007–15 Dec 2007	Multiple	3, 13

reader. First, we present a realization of the submesoscale regime on the shelf with a picture of an instantaneous 2-h average to motivate the rest of the study. Figure 3 illustrates the abundance of ephemeral submesoscale coherent structures on the shelf in the ROMS simulation of Santa Monica and San Pedro Bays.[3] Spatially heterogeneous coherent structures are evident inshore of and extending past the shelf break (roughly coincident with the 110-m isobath) as straight lines, curves, and spirals of strong cyclonic relative vorticity. The large, cyclonic $\zeta/f \gg 1$ associated with these structures, their nonuniform instantaneous spatial distribution, and corresponding advective evolution (seen in the animation in the supplemental material) identify these currents as submesoscale and differentiate them from lower Ro, spatially fixed tidal mixing and shelfbreak fronts. Coincident with these vorticity structures are surface convergence structures (Fig. 3c) as well as large surface buoyancy gradients (Figs. 3b,d). By continuity, the strong surface convergence indicates strong downwelling. The surface convergence and associated downwelling is a signature of the ageostrophic secondary circulations of these features (section 5e). The buoyancy gradients can be classified as fronts (transverse steps in buoyancy) or filaments (transverse extrema in buoyancy). Dense (cold) filaments are more prevalent than light (warm) filaments because of the direction and effect of the secondary circulation on maintaining the surface buoyancy gradient: the secondary circulation of a cold filament acts to strengthen the surface buoyancy gradient with convergence and downwelling at its center, whereas the secondary circulation associated with a warm filament inhibits strengthening of the surface buoyancy gradient with divergence and upwelling at its center (McWilliams et al. 2009a).

We highlight three diverse types of structures indicated by the boxed regions in Fig. 3b (from left to right): dense-core vortices with cross-shore extending filaments, a midshelf front that runs roughly parallel to local bathymetry (referred to as Front2; Table 2), and a cross-isobath-oriented dense filament connected to a "fork" of two fronts intersecting the shoreline. All of the isolated features (in Fig. 3 and in the rest of the study) are identified as submesoscale structures by their strong cyclonic vorticity, strong surface convergence, and associated downwelling, extreme lateral buoyancy gradients, and an O(hours–days) life cycle; the advective evolution of the submesoscale coherent structures distinguishes them from inertia–gravity waves emitted in the L3 solution that also exhibit large relative vorticity and divergence values.

The particular 2-h-averaged realization in Fig. 3 shows a somewhat isotropic orientation of the fronts and filaments whose longitudinal axis can be either parallel or perpendicular to isobaths. In the subsequent section 5b, we show that there is a preference of orientation of fronts and filaments relative to isobaths, a preference that is more strongly expressed closer to shore.

a. Regional heterogeneity

We investigate the regional distribution of submesoscale activity by analyzing metrics for submesoscale-indicating fields at the surface: relative vorticity $[\zeta = (\partial v/\partial x) - (\partial u/\partial y)]$ and divergence $[\delta = (\partial u/\partial x) + (\partial v/\partial y)]$. Strong signals in any of the latter variables are indicative of submesoscale coherent structures (fronts, filaments, and vortices; Fig. 3). Specifically, metrics that reveal imprints of strong cyclonic surface vorticity and surface convergence are indicative of the more persistent downwelling fronts and filaments.

Spatial heterogeneity (primarily through topographic control) is revealed in the variance maps for both fields ζ/f, δ/f in Figs. 4a and 4b. The strongest variance (most strikingly for ζ/f) is at the headlands and inside of Long Beach Harbor because of vortical wakes generated by flow through the breakwaters. On the shelf, there is a clear tendency for submesoscale variance to trace

[3] The supplemental material contains an animation (https://youtu.be/STJ4PMKUj5g) with visual evidence of the ubiquity of these features.

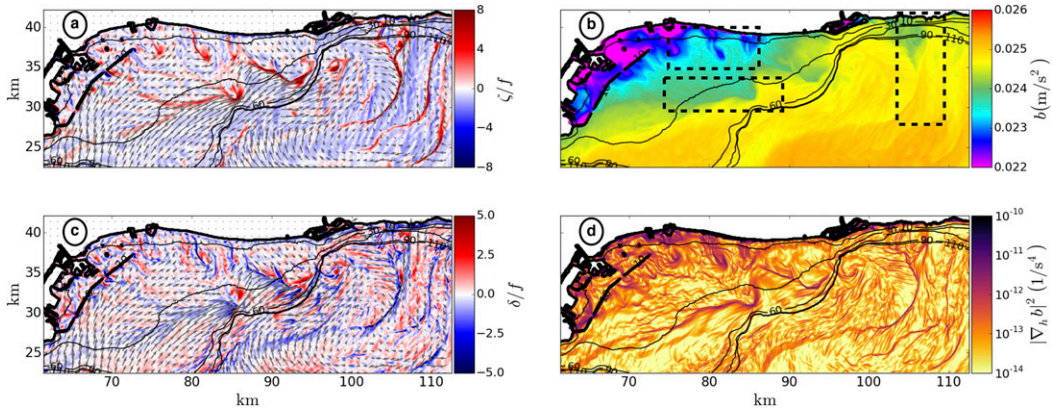

FIG. 3. Instantaneous 2-h average of surface fields in San Pedro Bay at 1300 PST 14 Dec 2007 from the L3 ROMS simulation. (a) Relative vorticity normalized by the Coriolis frequency (colors) and surface horizontal velocity vectors (arrows). (b) Buoyancy ($b = -g\rho/\rho_0$). (c) Divergence normalized by the Coriolis frequency (colors) and surface horizontal velocity vectors (arrows). (d) Horizontal buoyancy gradient magnitude (squared; log color scale). Solid black lines indicate bathymetry. Dashed boxes in (b) highlight certain features discussed in the text. Specifically, the midshelf front running parallel to the shoreline is referred to as Front2 in section 5f.

isobaths, with most of the activity occurring in between the 20- and 100-m isobaths. The tendency of vorticity variance to follow isobaths is broken in Redondo Canyon in SMB (Fig. 2b), where a roughly cross-shore signal extends from the shelf all the way offshore; this is potentially a pathway for strong vorticity structures to exit the SMB shelf. Relative to offshore regions, the shelf clearly has stronger variance and spatial heterogeneity. However, a relatively quiet nearshore region does exist on the broad SPB shelf, just southeast of Long Beach Harbor.

Skewness maps for vorticity and divergence (Figs. 4c,d) show the spatial distribution of the asymmetry of the PDFs for ζ/f or δ/f calculated at each grid cell for all time points (1812 samples). A positive ζ/f (δ/f) skewness value indicates a preference for cyclonic (divergent) motion and vice versa. The spatial distribution of skewness in the domain is made up of many near-grid-scale bands of large skewness magnitude. Our interpretation is that these bands indicate the repeated passage of multiple like-signed, high-magnitude vorticity (e.g., $\zeta/f \gg 1$) and divergence (e.g., $\delta/f \ll -1$) structures over neighboring grid cells. Offshore of the shelf break, these patterns are rather isotropic in orientation, and nearshore there is more evidence of topographic control. Overall, the maps show a cyclonic (positive ζ/f skewness) and convergent (negative δ/f skewness) preference at the surface, as expected from the standard view of fronts and filaments (McWilliams 2016).

Negative vorticity skewness is present on the northwestern side of each headland (Palos Verdes and Point Dume). The anticyclonic vorticity generation at these headlands is most likely due to the mean alongshore current located offshore (counter to the equatorward California Current) that generally advects warm water to the north and west along the coast in the SCB. Also, the harbors on the shoreline exhibit cyclonic and anticyclonic vorticity generation (most strikingly at Long Beach Harbor in the gaps of the breakwater), partly because of tidal vorticity generation. The positive vorticity skewness on the SPB shelf is diminished near the shoreline (roughly shoreward of the 20-m isobath), and there is nonnegligible anticyclonic skewness in that region potentially related to the generation of anticyclonic structures in Long Beach and Newport Harbors. Apart from the nearshore topographic influences on the skewness maps of vorticity and divergence, the spatial distribution of skewness in the regions offshore of the shelf break exhibit a collage of near-grid-scale cyclonic (Fig. 4c, red shading) or convergent (Fig. 4d, blue shading) bands or zones. An exception to this offshore isotropy is the Redondo Canyon streaks that extend offshore from the shelf (Fig. 4c). Shcherbina et al. (2013) gives observational evidence of the cyclonic, convergent skewness in submesoscale-resolving measurements of open-ocean surface currents, but the interpretations of spatial distribution given in Figs. 4c and 4d have not been applied to an open-ocean setting.

Buijsman et al. (2012) show that there is an active internal wave field in the SCB, and we expect such activity in the L3 solution. Internal waves can provide a source of large vorticity and divergence in the L3 solution and may dilute the signals in Fig. 4 interpreted as indicative of submesoscale dynamics. However, the SI animation of the surface flow fields shows a dominance of the largest vorticity and divergence signals under advective evolution (i.e., submesoscale coherent

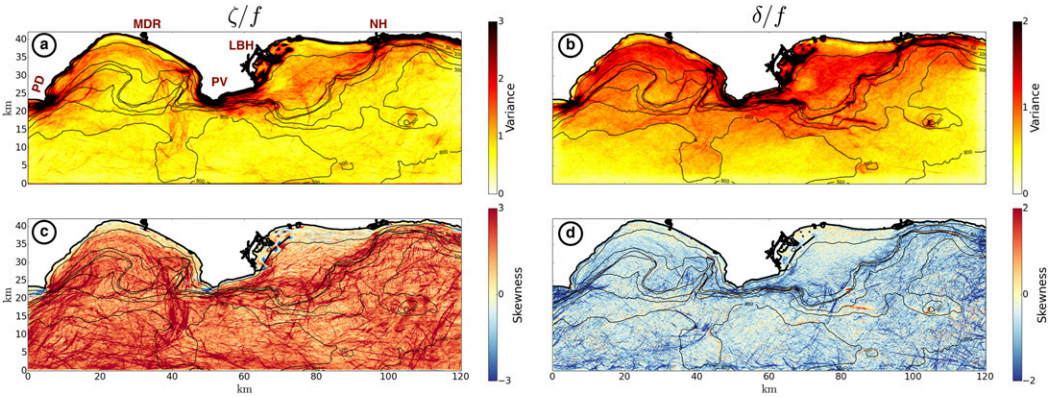

FIG. 4. (top) Variance and (bottom) skewness for surface (left) relative vorticity and (right) divergence normalized by the Coriolis parameter f. Variance and skewness are calculated at each grid cell from 151 days of velocity output averaged at 2-h intervals (1812 total time points). Solid black lines indicate bathymetry. The variance color bar is oversaturated near the shoreline. Marina Del Rey (MDR), Long Beach Harbor (LBH), Newport Harbor (NH), and the Point Dume (PD) and Palos Verdes (PV) headlands are denoted in (a) to orient the reader.

structures) while capturing tidal variability (a primary driver of internal wave generation); the metrics of Fig. 4 are obtained from 2-h-averaged surface fields and will predominantly capture these advectively dominated surface dynamics with some, but not overwhelming, dilution by the internal wave field, which will be more expressed in the interior.

b. Spatial orientation of fronts and filaments

The variance maps in Figs. 4a and 4b indicate a shallow-water preference for high vorticity variance to align parallel to isobaths (most strongly in SMB). We investigate this cross-shelf preference of submesoscale structures further by examining the angle of extreme density gradients (uniquely associated with strong fronts and filaments) relative to depth (indicating cross-shore location). Probability density functions (PDFs) of surface density gradient vector magnitude ($|\nabla_h \rho|$) and angle ($\theta_{\nabla_h \rho}$) are calculated for all 151 days of the simulation (1812 temporal data points) and organized relative to the bottom depth of the sampling location. PDFs are obtained from 300 (x, y) sampling locations along a specific isobath. The sampling locations are chosen to span the longest alongshore contour of an isobath; that is, sampling locations are not placed on small closed contour areas (e.g., a seamount). We use 90 isobaths in our analysis spanning $h \in [10, 900]$ m at 10-m intervals.

The density gradient vectors are rotated into a local coordinate frame relative to the bathymetric gradient [analogous to the coordinate transformation in Romero et al. (2013)]. The transformation is made such that the cross-shelf axis x' is parallel to the bathymetric gradient and the along-shelf axis y' is oriented 90° counterclockwise to the cross-shelf axis. Using the bathymetric unit gradient vector $\mathbf{h}_g = \nabla h/|\nabla h| = \mathbf{h}_x + i\mathbf{h}_y$, the density gradient vector is decomposed into along- and cross-shelf components:

$$\frac{\partial \rho}{\partial x'} = \frac{\partial \rho}{\partial x}\mathbf{h}_x + \frac{\partial \rho}{\partial y}\mathbf{h}_y, \quad \text{and}$$
$$\frac{\partial \rho}{\partial y'} = \frac{\partial \rho}{\partial y}\mathbf{h}_x - \frac{\partial \rho}{\partial x}\mathbf{h}_y, \tag{4a}$$

where x and y represent the horizontal geographical axes of the model domain in Fig. 2b. The direction of the density gradient relative to bathymetric gradient is given by

$$\theta_{\nabla_h \rho} = \tan^{-1}\left(\frac{\partial \rho/\partial y'}{\partial \rho/\partial x'}\right). \tag{5}$$

Here, $\theta_{\nabla_h \rho} = -\pi, 0, \pi$ translates to a density gradient pointing across isobaths, with $\theta_{\nabla_h \rho} = 0$ implying a density gradient pointing in the same direction as the bathymetric gradient (i.e., offshore).

Figure 5a shows the PDF of density gradient magnitude at each isobath. There is a clear difference in the breadth of the PDFs for shallow and deep water. In shallower water (10–100 m), PDFs of $|\nabla_h \rho|$ are broader relative to the PDFs in deeper water (>100 m). This dependency in PDF shape as a function of depth implies that there are stronger density gradients in the nearshore, potentially because of the combination of the weaker stratification and stronger velocity gradients (i.e., stronger ζ/f, δ/f variance in the nearshore in Figs. 4a,b).

Figure 5b shows the PDFs of the orientation angle ($\theta_{\nabla_h \rho}$) for each isobath. We isolate the front and filament density gradients (i.e., strongest gradient magnitudes) by conditionally sampling the gradient vectors that exceed 5 times the RMS of the density gradient magnitude

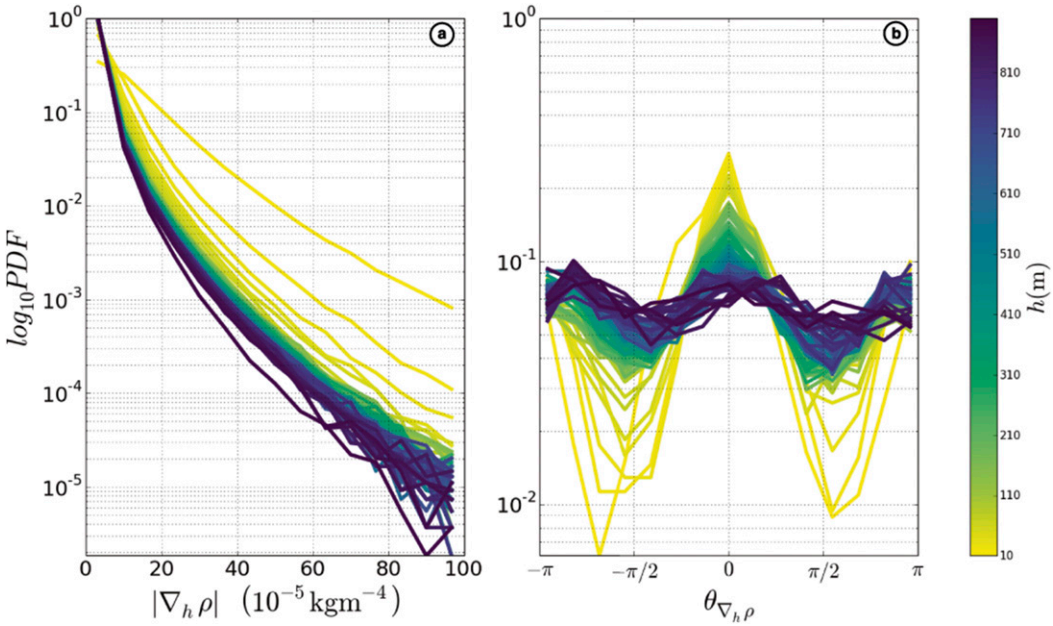

FIG. 5. PDFs ($\log_{10}$) of (a) surface density gradient vector magnitude and (b) angle relative to different isobaths (colors). Each PDF of surface density gradient magnitude $|\nabla_h\rho|$ is calculated from 300 points along each isobath for all 151 days of simulation. The PDFs of the density gradient angles $\theta_{\nabla_h\rho}$ are obtained from density gradient vectors in which the magnitude exceeds 5 times the RMS value of $|\nabla_h\rho|$ (RMS is relative to data points along a specific isobath). Angle conventions are such that $\theta_{\nabla_h\rho} = -\pi$, 0, π correspond to the density gradient vector pointing across isobaths. Note that depth h is indicated as a positive value here (opposite to the convention in Fig. 2)

relative to data points along each isobath; the curves in Fig. 5b give a metric of preferred alignment of surface fronts and filaments relative to depth. Analogous to the strength of $|\nabla_h\rho|$, there is a clear dichotomy in preferred horizontal orientation between the shallow and deep regimes. Strong density gradients in shallow-water preferentially point across isobaths directed toward deeper water ($\theta_{\nabla_h\rho} = 0$). This implies a front or filament that has its longitudinal axis aligned parallel to isobaths. This preference is diminished as depth increases (flattening of the PDFs in darker colors). Analogously, there is a clear inhibition of nearshore fronts and filaments aligned across isobaths ($\theta_{\nabla_h\rho} = -\pi/2$, $\pi/2$).

These results corroborate the interpretations from the variance maps in Figs. 4a and 4b; there is more extreme submesoscale activity (velocity and density horizontal gradients) closer to shore with the alignment and regional distribution of structures closer to shore controlled by regional bathymetry. Typically, the strongest flows associated with fronts and filaments are a (mainly) geostrophic longitudinal shear flow. On the shelf, this flow can extend to or near the bottom because of the weak stratification and strong vertical mixing (section 5e). Shelf bathymetry can orient fronts and filaments by steering the associated longitudinal flow along isobaths. Another, perhaps secondary, degree of control lies in the interaction of the shape of the coastline with mean flows. The baywide regions of high vorticity and divergence variance show even larger variance at the headlands (Figs. 4a,b). Background alongshore flows associated with vorticity generation at headlands could continually favor along-isobath alignment of headland-rooted submesoscale coherent structures.

c. *Frontogenetic tendencies*

In the realistically complex situation in our simulation, all of the submesoscale generation processes (section 3) are likely to occur. Rather than attempt to untangle these three different mechanisms, we investigate the processes responsible for frontogenesis, that is, what causes $|\nabla_h b|^2$ and $|\nabla_h \mathbf{u}|^2$ in submesoscale structures on the shelf. Does the formation of shelf coherent structures mirror the formation of open-ocean analogs or does the topographic control on spatial distribution and alignment exert itself in the formation process as well?

To aid our interpretation in ‘‘catching’’ the precise moment of formation of a shelf filament, we use 30-min-averaged output of L3 solutions over a period of 2 days during a cold filament’s life cycle. The rapid growth and elongation of this cold filament is shown as it forms near Newport Harbor in Figs. 6a–d. We refer to this filament as Filament1. We illustrate the formation of the filament

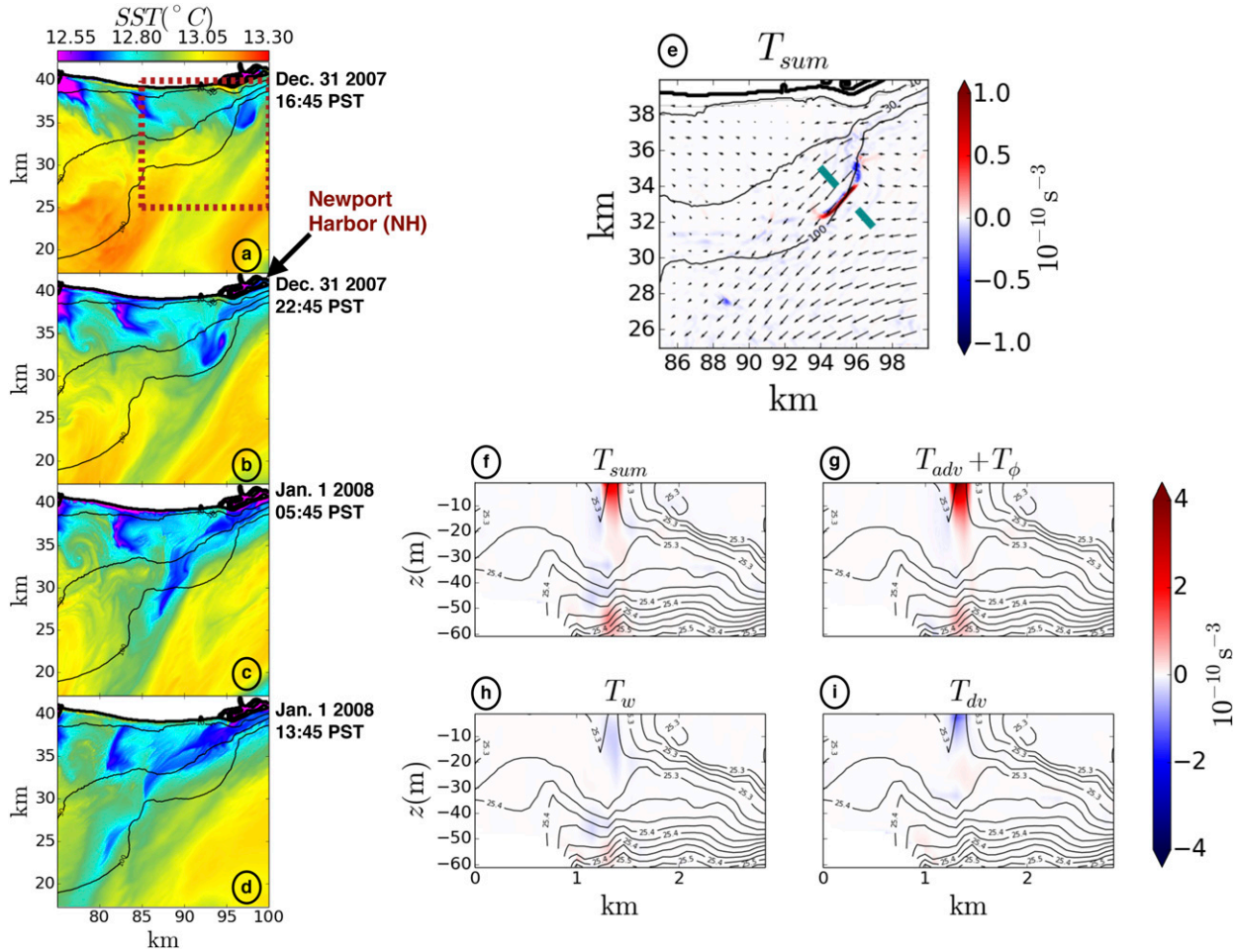

FIG. 6. Frontogenesis of Filament1. (a)–(d) Instantaneous 30-min averages of SST beginning on 1645 PST 31 Dec 2007. (e) Total velocity gradient frontogenetic tendency for the region in the red dashed box in (a) at $z = -5$ m. (f)–(i) Separate frontogenetic terms for the transverse cross section with end points denoted by the cyan hash marks in (e). Black vectors in (e) denote horizontal velocity at $z = -5$ m and black contours in (f)–(i) denote density.

in SST, noting that there is an analogous signal in sea surface salinity (SSS). A cold, salty (relative to its surroundings) cyclonic vortex exists on the very narrow shelf off of Newport Harbor. In the sequence, there is a clear stretching and elongation of the cold patch just off of the shelf break, which is the result of the horizontal strain field acting on the buoyancy gradient.

We quantitatively diagnose the specific processes responsible for front or filament formation through the frontal tendency equations. The usual practice is to decompose the terms responsible for amplification of the buoyancy gradient in time $(1/2)[(D|\nabla_h b|^2)/Dt]$, as in Hoskins (1982), Capet et al. (2008c), and Gula et al. (2014). However, for filament frontogenesis it is informative (and more striking visually) to look at the evolution of the velocity gradient $(1/2)[(D|\mathbf{\nabla}_h(u,v)|^2)/Dt]$ (following McWilliams et al. 2015):

$$\frac{1}{2}\frac{D}{Dt}\begin{pmatrix}|\mathbf{\nabla}_h u|^2\\ |\mathbf{\nabla}_h v|^2\end{pmatrix} = \sum_i \begin{pmatrix}T_{i,u}\\ T_{i,v}\end{pmatrix} = \sum_i \begin{pmatrix}\mathbf{Q}_{i,u}\cdot\mathbf{\nabla}_h u\\ \mathbf{Q}_{i,v}\cdot\mathbf{\nabla}_h v\end{pmatrix}, \qquad (6)$$

where $T_{i,u}$, $T_{i,v}$ represent individual frontogenetic tendency terms that account for a physical process inherent in the momentum equation (i = horizontal advection, vertical advection, vertical mixing, etc.) that can contribute to amplification ($T_i > 0$, frontogenetic) or reduction ($T_i < 0$, frontolytic) of the velocity gradient ($|\mathbf{\nabla}_h u|^2$ or $|\mathbf{\nabla}_h v|^2$). For this analysis, we present the frontogenetic tendency for the velocity gradient T_i as the sum of the tendencies for the individual u and v gradients ($T_i = T_{i,u} + T_{i,v}$), where individual processes contributing to frontogenetic or frontolytic behavior are accounted for by the $\mathbf{Q}_i$ vector. These processes are horizontal advection $\mathbf{Q}_{\mathrm{adv}}$, vertical advection $\mathbf{Q}_w$,

Coriolis conversion $\mathbf{Q}_f$, pressure gradient $\mathbf{Q}_\phi$, vertical mixing $\mathbf{Q}_{\mathrm{dv}}$, and horizontal diffusion $\mathbf{Q}_{\mathrm{dh}}$. They are defined as follows [written as (u, v) components]:

$$(\mathbf{Q}_{\mathrm{adv},u}, \mathbf{Q}_{\mathrm{adv},v}) = (-u_x \nabla_h u - u_y \nabla_h v, -v_x \nabla_h u - v_y \nabla_h v), \tag{7a}$$

$$(\mathbf{Q}_{w,u}, \mathbf{Q}_{w,v}) = (-u_z \nabla_h w, -v_z \nabla_h w), \tag{7b}$$

$$(\mathbf{Q}_{f,u}, \mathbf{Q}_{f,v}) = (f \nabla_h v + v \nabla_h f, -f \nabla_h u - u \nabla_h f), \tag{7c}$$

$$(\mathbf{Q}_{\phi,u}, \mathbf{Q}_{\phi,v}) = [\nabla_h(-\phi_x), \nabla_h(-\phi_y)], \tag{7d}$$

$$(\mathbf{Q}_{\mathrm{dv},u}, \mathbf{Q}_{\mathrm{dv},v}) = \left\{ \nabla_h \left[\frac{\partial}{\partial z} \left(\kappa_v \frac{\partial u}{\partial z} \right) \right], \nabla_h \left[\frac{\partial}{\partial z} \left(\kappa_v \frac{\partial v}{\partial z} \right) \right] \right\}, \tag{7e}$$

and

$$(\mathbf{Q}_{\mathrm{dh},u}, \mathbf{Q}_{\mathrm{dh},v}) = \nabla_h (D_{hu}, D_{hv}). \tag{7f}$$

In Figs. 6e–i (and later Figs. 7h–l), the tendency term for horizontal diffusion T_{dh} is not shown knowing that it is always frontolytic in ROMS because of the implicit hyperdiffusion D_h associated with the upstream advection operator (Gula et al. 2014). Similarly, we do not show T_f, which represents an exchange between the u and v components and will sum to zero except for a small term $\propto \beta = df/dy$. For a purely geostrophic flow, T_ϕ and T_{adv} are each zero. At higher order in Rossby number, the pressure field is often closely related to horizontal momentum advection, so we choose to show a combined $T_{\mathrm{adv}} + T_\phi$ (as opposed to each individually) to interpret horizontal advective effects; we note that T_ϕ is similar in structure and lesser in magnitude than T_{adv} for the cases shown. Analysis of the terms controlling the buoyancy gradient frontogenetic tendency $(1/2)[(D|\nabla_h b|^2)/Dt]$ (not shown) leads to similar conclusions about the relevant processes.

The total frontogenetic tendency is shown at $z = -5$ m in Fig. 6e, corresponding to Filament1 at the time in Fig. 6a. There is a clear positive frontogenetic tendency indicative of a drastic increase in velocity gradient. The separate terms that contribute to this tendency are shown for a cross section at the same time in Figs. 6f–l. Horizontal advection T_{adv} $(+T_\phi)$ contributes the most to the frontogenesis. The terms T_w, T_{dv} are frontolytic around the center of the filament.

The strong frontogenetic horizontal advective tendency, confined to a ~10-m-thick surface layer (Fig. 6g), indicates that the surface layer horizontal flow structures surrounding the filament are responsible for its growth (rapid amplification of $|\nabla_h \mathbf{u}|^2$; Fig. 6e). Offshore of the 100-m isobath, a convergent flow pushes the nascent filament into shallower water. Inshore of the 100-m isobath, the large-scale flow strains the filament along isobath to the southwest. The convergence by the offshore flow and strain by the inshore flow act to elongate and amplify both the velocity and buoyancy gradient in a mixture of the Hoskins (1982) deformation flow and McWilliams et al. (2015) convergent secondary circulation mechanisms of frontogenesis. The relatively large submesoscale activity (Figs. 4a,b) and large horizontal strain $\left[S = \sqrt{(u_x - v_y)^2 + (v_x + u_y)^2}\right]$ variance (not shown) near Newport Harbor indicate that the formation of submesoscale density gradients, driven by the favorable alignment of flows off- and inshore of the 100-m isobath (Fig. 6e), is not an anomalous event in this region. The orientation of the local bathymetry and coastline surrounding Filament1 may topographically steer large-scale flow fields in a way that favors repeated generation of submesoscale structures in this area near the shelf break.

The general picture from Fig. 6 is filament formation driven mainly by frontogenetic horizontal advection with simultaneous but weaker frontolytic vertical advection and vertical mixing; it generally agrees with the Gulf Stream filament formation analyzed in Gula et al. (2014). However, the orientation of the shelf bathymetry relative to the coastline exerts some control on the frontogenetically favorable ambient flow configurations, and the shallow depth can lead to nontrivial frontogenetic tendencies near the bottom. The surface-driven, advectively dominated formation mechanism of this submesoscale density gradient is distinct from the BBL-associated formation mechanisms for shelfbreak and tidal mixing fronts. It is distinct from both the frontal trapping formation mechanism of shelfbreak fronts (Chapman and Lentz 1994) and the formation of tidal mixing fronts that fundamentally involves tidally induced vertical mixing (Simpson and Hunter 1974).

d. *Influence of the coastline: A headland wake event*

The formation of Filament1 is essentially controlled by the surface flow field and is somewhat analogous to formation of open-ocean filaments (Gula et al. 2014). However, the ambient flow frontogenesis for Filament1 seems to be controlled by the interaction of large-scale flows and the orientation of the shelf bathymetry relative to the coastline. As revealed by the metrics in Figs. 4 and 5, the shape of the coastline and bathymetry are important influences on the regional heterogeneity of submesoscale processes on the shelf. Specific areas along the coastline can act as formation sites for submesoscale structures (e.g., headlands and breakwaters).

A striking illustration of the influence of the coastline is shown in the simultaneous formation of a cold-core vortex

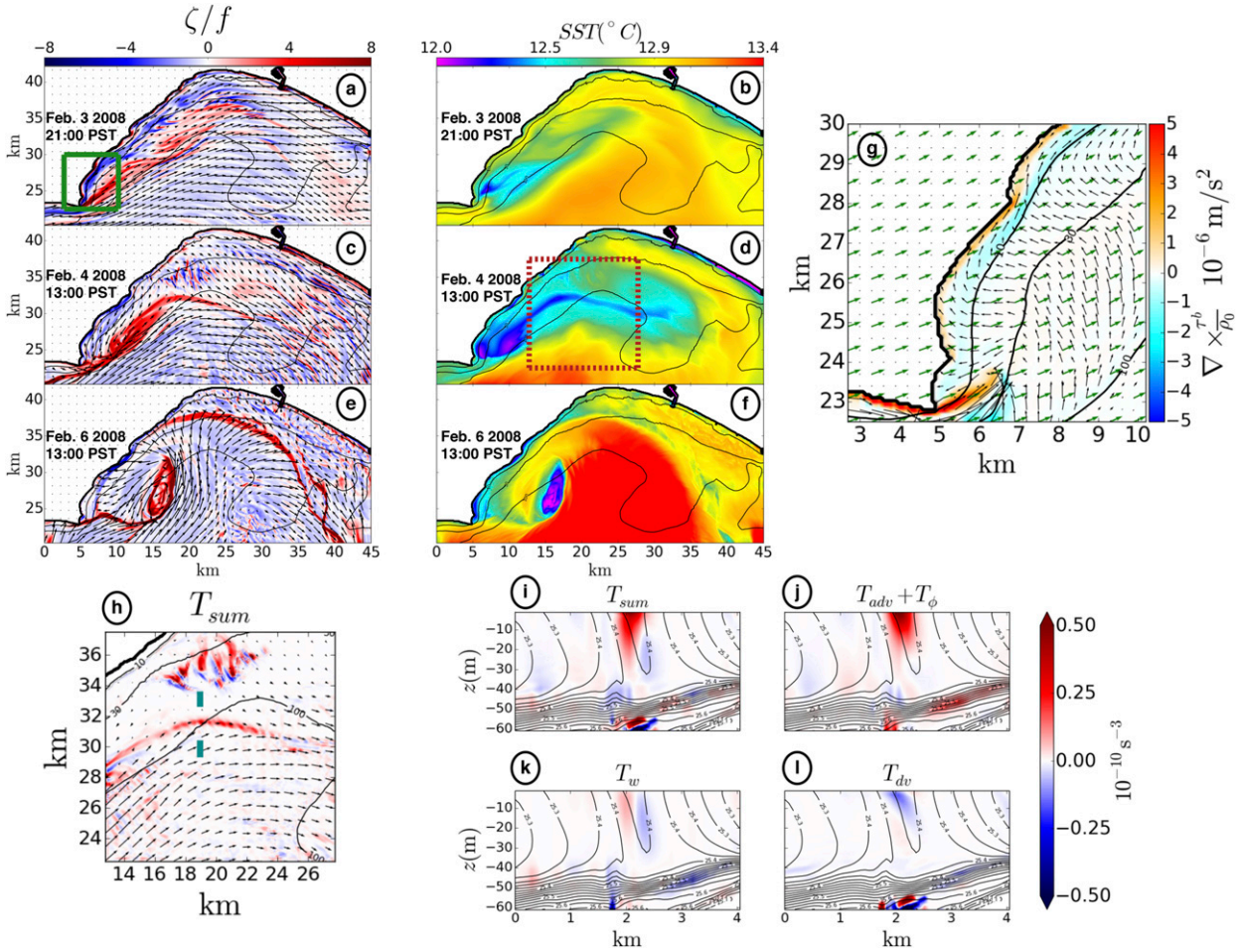

FIG. 7. Headland wake frontogenesis of Filament2. Instantaneous 2-h averages of (a),(c),(e) surface relative vorticity and (b),(d),(f) SST are shown for three separate times (rows, beginning on 2100 PST 3 Feb 2008; note uneven times between second and third rows). (g) Curl of the bottom stress (colors), surface wind stress (green vectors) and, bottom velocity (black vectors) of the green region in (a). (h) Total velocity gradient frontogenetic tendency for the region in the red dashed box in (d) at $z = -5$ m. (i)–(l) Separate frontogenetic terms for the transverse cross section with end points denoted by the cyan hash marks in (h). Black vectors in (a), (c), and (e) denote surface horizontal velocity and in (h) denote horizontal velocity at $z = -5$ m. Black contours in (i)–(l) denote density.

and cold filament in Fig. 7 at the Point Dume headland (referred to as Filament2). The sequence of events in this figure is a combination of the following processes: shallow-water wake formation caused by horizontally varying bottom drag (Fig. 7g), upwelling caused by wind stress curl, and filament frontogenesis mainly driven by horizontal advection (Figs. 7i–l). The initial cyclonic vorticity in Fig. 7a can primarily be explained by highly localized vertical vorticity generation caused by bottom drag ($\nabla \times \boldsymbol{\tau}^b > 0$), which is due to strong mean flow past the headland (Fig. 7g). The upwelling of cold, salty water at the headland is in part due to upwelling-favorable wind stress curl. The wind stress is shown in green arrows in Fig. 7g, and the upwelling is also indicated by the onshore bottom flow (black arrows Fig. 7g) intersecting the coastal boundary. The cyclonic vorticity created by the bottom drag fits the mechanism invoked in shallow-water island wake formation (Wolanski et al. 1984; Tomczak 1988; Furukawa and Wolanski 1998) and in the flow along a sloping bottom (Molemaker et al. 2015). The horizontal shear created by the eastward flow in contact with the headland, the upwelling of denser water in the lee of the headland, and topographic steering within SMB gives rise to the fully evolved coherent structures of a cold-core vortex and a cold filament that roughly traces out baywide bathymetry (Figs. 7c–f). Notice the detachment of the vortex from the headland and the separation of the filament from the vortex in Figs. 7e and 7f. While Filament2 is an example of a cyclonic coherent structure, the surface vorticity skewness map in Fig. 4c shows small patches of anticyclonic vorticity generation to the west of both headlands, associated with episodes of westward flow.

The frontogenetic tendencies of Filament2 are analyzed in Figs. 7h–l. Analogous to the result for Filament1, horizontal advection T_{adv} $(+T_{\phi})$ is positive and dominates the sum of the frontogenetic tendency. Cross sections of the separate terms (Figs. 7i–l) show that T_{dv} is mainly frontolytic, with a very weak frontogenetic tendency on the inshore side of the filament nearest the surface. The term T_w is sign symmetric around the center of the filament. Overall, horizontal advection takes over the frontogenetic sequence after the initial cyclonic vorticity creation, which is fundamentally controlled by the shape of the coastline. This sequence of events is unique to coastal submesoscale density gradients and has no analog in the open-ocean surface layer.

e. *Front and filament circulations*

Here, we present both the success and limitation of the TTW balance [(1)] in diagnosing the circulations associated with fronts and filaments on the shelf. Motivated by an example of the failure of the TTW diagnostic, we investigate the transient evolution of secondary circulations and raise questions regarding the steady-state assumption inherent in the TTW diagnostic.

For the finite-depth shelf, we impose the following boundary conditions on (1):

$$\kappa_v \frac{\partial \mathbf{u}_h}{\partial z} = \frac{\boldsymbol{\tau}^s}{\rho_0} \quad \text{at} \quad z = 0, \qquad \kappa_v \frac{\partial \mathbf{u}_h}{\partial z} = \frac{\boldsymbol{\tau}^b}{\rho_0} \quad \text{at} \quad z = -h. \quad (8)$$

The inclusion of a bottom stress $\boldsymbol{\tau}^b$ is specific to shelf fronts and filaments that are commonly in contact with the bottom because of the combination of the shallow depths [$O(10)$ m] and low stratification induced by the strong mixing that sets up and maintains the secondary circulations. The stress $\boldsymbol{\tau}^b$ is computed from the L3 solution bottom sigma-level velocity using the bottom-layer quadratic drag law given by (3).

The TTW longitudinal u and transverse v velocities can be calculated from ROMS output with knowledge of the density ρ, vertical mixing κ_v, surface wind stress $\boldsymbol{\tau}^s$, and, on the shelf, the bottom velocity $\mathbf{u}_b$. Discretization of (1) results in a tridiagonal system and can be solved by a simple matrix inversion if the coefficient matrix is diagonally dominant. The discretization is analogous to that of McWilliams et al. (2015) with the inclusion here of a bottom stress in the bottom boundary condition.

1) EXAMPLES OF TTW BALANCE

To investigate this mechanism for shallow-water fronts and filaments in contact with the bottom, we isolate three submesoscale features shown in Fig. 8: Filament3, Filament4, and Front1. The input fields for the calculation (κ_v, $\boldsymbol{\tau}^s$, $\boldsymbol{\tau}^b$, ρ) are obtained by isolating the submesoscale feature at the locations denoted by the black hash marks in Fig. 8. Front1 is shown in Fig. 8 at two times (bottom two rows) to show an example of diurnal evolution discussed in the next subsection. The TTW input fields and solutions (Figs. 9, 10, 11) are shown as longitudinal averages in the transverse-depth (y–z) plane.

The first case, Filament3, is a cold filament [isolated at 0300 Pacific standard time (PST)] located just offshore of Manhattan Beach roughly between the 10- and 50-m isobaths (top row, Fig. 8). In the nearshore, the filament is oriented at roughly a 45° angle to the 10-m isobath and bends to a more along-isobath parallel orientation farther offshore and toward the south (to the right along the horizontal axis). It has a sharp temperature gradient with strong cyclonic vorticity and convergence at the surface. Figures 9a and 9b show transverse-depth structure (longitudinally averaged) of density $\rho(y, z)$ and parameterized vertical mixing $\kappa_v(y, z)$. The two main ingredients for the TTW circulation are apparent: a strong horizontal density gradient (not explicitly shown) across the transverse axis (roughly uniform from the surface down to about −35-m depth) and strong $O(10^{-2})$ m s^{-2} vertical mixing. Of note is the trend in κ_v to decrease in strength in shallower water. This is a general, statistical cross-shore trend explained by the influence of the decreasing depth; the magnitude of κ_v (produced by KPP) is primarily controlled by boundary layer depth (here interpreted as depth of the water column). We also note that this filament occupies both the continental shelf (separate SBL and BBL) and the SSTZ (overlapping SBL and BBL) of Fig. 1.

Velocities for Filament3 are shown in Figs. 9c and 9d after being rotated into a filament frame of reference. The circulation is characterized by a cyclonically sheared longitudinal flow and a transverse circulation that is convergent at the surface and divergent at depth (the secondary circulation). Geostrophic balance ($u_g = -\phi_y/f$, $v_g = \phi_x/f$) fails to reproduce the complete structure of this transverse flow (Figs. 9e,f) and also does not fully capture the extent of vertical mixing of the longitudinal flow. The ageostrophic secondary circulation is better captured by the TTW balance (u_{TTW}, v_{TTW}; Figs. 9g,h). This result is analogous to the TTW success for open-ocean filaments in Gula et al. (2014) and provides a validation of the TTW balance in shallow water with overlapping boundary layers.

Front1 is a shelf front located off of Long Beach Harbor in SPB (isolated at 0400 PST; third row, Fig. 8). The front is characterized by colder water offshore and warmer water onshore, with very well-defined lines of cyclonic vorticity and surface convergence coincident with the location of maximum temperature gradient. The TTW diagnostic is moderately successful (relative to Filament3) in recreating the longitudinal shear flow as well as the ageostrophic secondary circulation (Fig. 10). There are

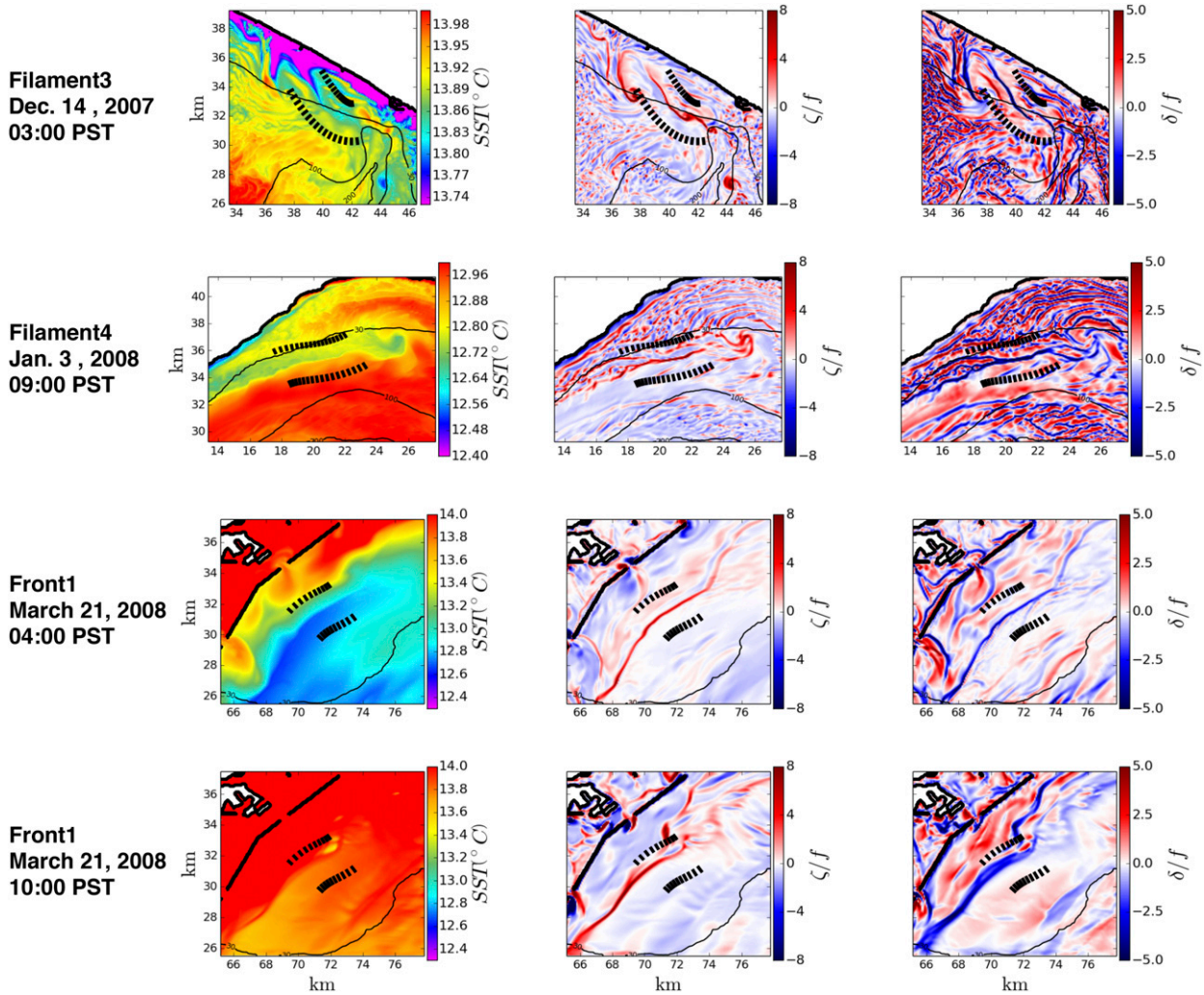

FIG. 8. Surface fields for the fronts and filaments (rows) used for TTW diagnostic calculation. (left) SST, (center) relative vorticity, and (right) divergence. The features are isolated by fitting a polynomial curve to the shape of the cyclonic vorticity line indicating the front or filament. Transverse cross sections 3 km in length are taken between the end points indicated by the black hash marks and centered on the fitted curve. Velocities and stresses are then rotated into a frame of reference of the feature (x, y pertaining to longitudinal and transverse axes, respectively).

some differences between the raw and TTW transverse velocity profiles. Notably, there is a patch of negative transverse velocity on the far side of the y axis in the TTW profile. This coincides with (and is potentially the result of) both an increase in stratification, a decrease in κ_v, and decrease in $\partial\phi/\partial y$ (i.e., the ingredients for TTW).

Filament4 appears as a shelf front[4] (isolated at 0900 PST) in SMB offshore of Malibu (second row, Fig. 8), oriented roughly parallel to the local isobaths. There are two notable aspects of this case to mention relative to Filament3 and Front1. First, the vertical mixing shape (Fig. 11b) is markedly different for this case (at this point in time in the front's life cycle) than the previous two cases discussed (Filament3 and Front1). Second, the TTW balance does not (as) convincingly reproduce the very strong and apparent secondary circulation (Fig. 11d) associated with this front. The vertical mixing structure is weak at the surface because of increased stratification (Fig. 11a) caused by a positive solar heat flux associated with the daytime hour (0900 PST) of the feature isolation. BBL mixing is present on the inshore side of the filament where it comes in contact with the bottom with a reduced stratification on this inshore side.

This case is of interest because the raw transverse flow exhibits a clear and very strong secondary circulation

[4] Filament4 exhibits a frontal structure at this time; however, its time mean (Fig. 13) resembles a cold filament and thus we name it Filament4.

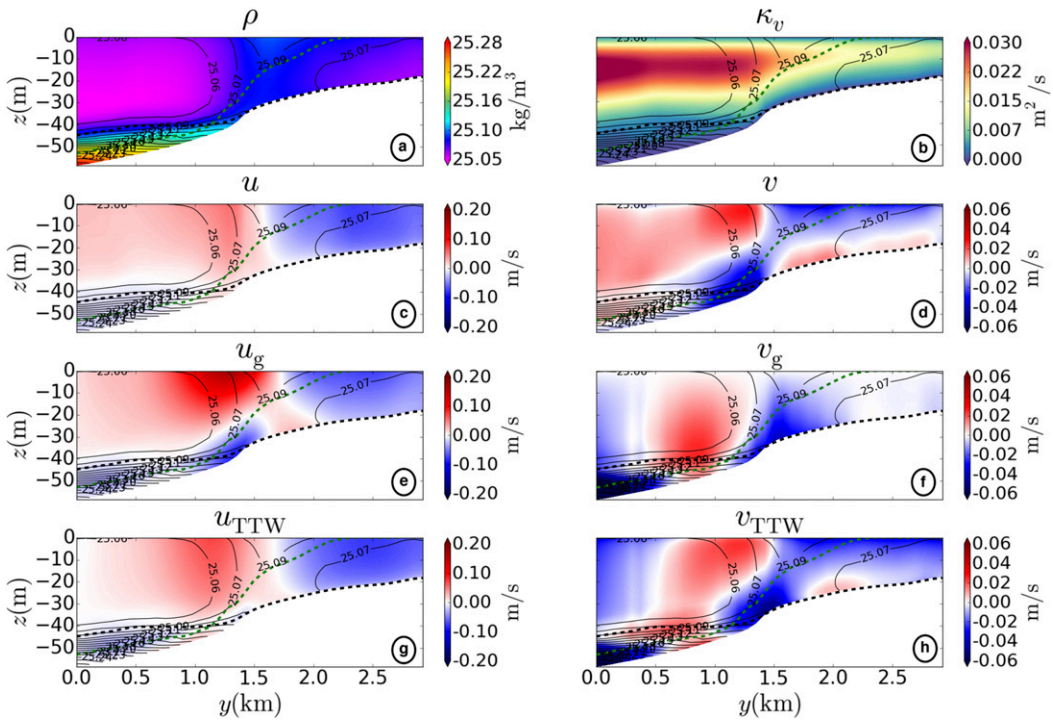

FIG. 9. Longitudinally averaged of fields for Filament3 cross sections: (a) density and (b) vertical mixing. Longitudinal velocity u and transverse velocity υ are shown in 3 components: (c),(d) raw,(e),(f) geostrophic, and (g),(h) TTW. Black contours denote density; dashed lines denote surface (black) and bottom (green) boundary layer depths. Bottom boundary layer depth is plotted relative to the bottom (i.e., vertical extent of bottom boundary layer). Sign conventions are such that positive u is out of the page and positive υ is to the right along the horizontal axis. For the TTW calculation itself, the pressure gradient in the longitudinal direction $\partial\phi/\partial x$ is modified to exclude the effect of larger-scale processes. This is done by setting the free-surface height η gradient in that direction to zero ($\partial\eta/\partial x = 0$) and calculating pressure with this modified free surface. There is also some spatial smoothing done to the transverse pressure gradient $\partial\phi/\partial y$. TTW velocities are computed for each horizontal cross section with the longitudinal composite of individual cross sections shown here; that is, we assume longitudinal uniformity of the front or filament circulation.

(Fig. 11d). However, the TTW diagnostic is not reproducing the strength and complete geometry of this secondary circulation (Fig. 11h). The presence of a strong secondary circulation coincident with relatively weak vertical mixing presents a conundrum for the diagnostic view of (1). Next, we investigate the transient evolution of submesoscale-indicating fields to show that the diurnal cycle in vertical mixing (presumably forced by solar heat flux or wind) induces a transient response of front and filament circulation that is apparently not captured by the steady-state TTW balance.

2) DIURNAL EVOLUTION OF SECONDARY CIRCULATION

We illustrate the diurnal evolution of secondary circulation (as it relates to cycling of κ_υ) with a 4-day time series of multiple fields in Fig. 12. The time series in Fig. 12 are spatial RMS values (normalized by their respective standard deviations in time) of fields at $z = -7$ m for a region indicated by dashed black lines in Fig. 2b; surface heat flux Q_s is plotted as a spatial mean. The diurnal cycling of κ_υ is apparent in Fig. 12. It is representative of the surface layer KPP response: KPP enhances vertical mixing at the surface via both a surface cooling ($Q_s < 0$) and/or a strong surface stress ($|\boldsymbol{\tau}^s| > 0$). The term κ_υ has a diurnal cycle characterized by sustained mixing in the nighttime hours (1700–0700 PST) followed by an abrupt transition to a low mixing regime during the day (0900–1500 PST). The stratification (N^2) diurnally evolves consistent with changes in κ_υ: stronger stratification with weaker mixing and vice versa (Fig. 12, gray curve).

The surface wind stress can certainly induce vertical mixing and potentially control the diurnal signal of Q_s through a diurnal sea breeze, which is common in Southern California (Nam and Send 2013). For SMB, the sea–land breeze phasing is a daytime onshore wind (ocean to land) and nighttime offshore wind. If the onshore breeze is strong enough during the daytime, it can increase and dominate

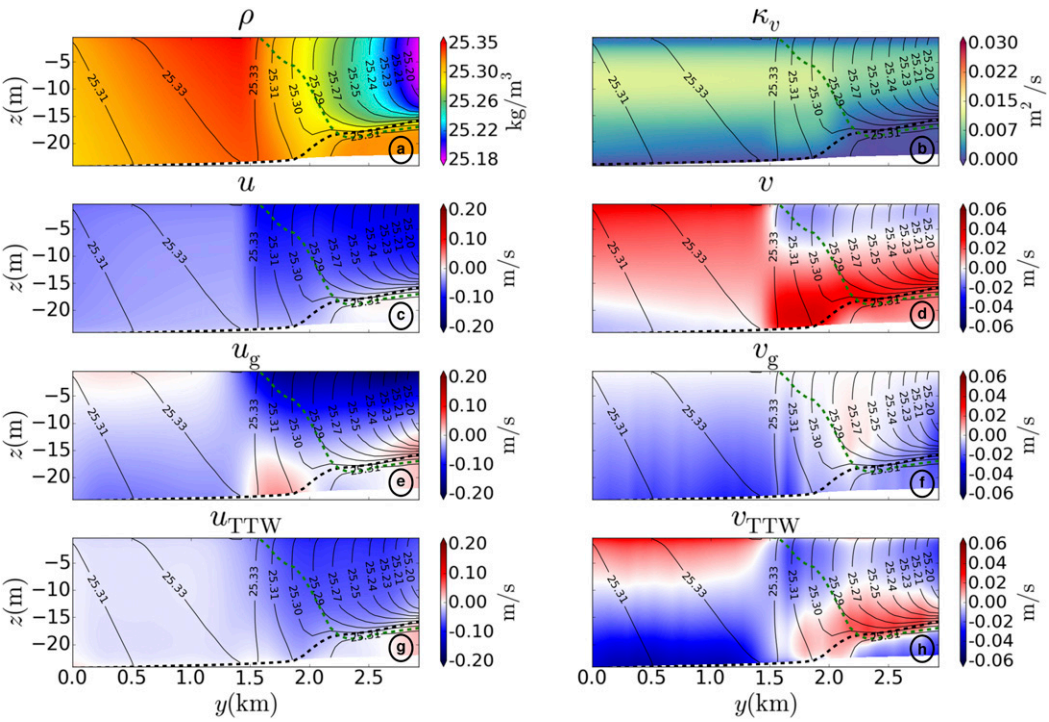

FIG. 10. As in Fig. 9, but for Front1 in Fig. 8

the vertical mixing (relative to stratifying effects of $Q_s > 0$ that can weaken the mixing). However, the most notable peaks in $|\boldsymbol{\tau}^s|_{\mathrm{RMS}}$ (the large peak of the orange curve in Fig. 12 at 2100 PST on 14 December) are due to a local wind event in Malibu with strong off- and alongshore winds that occur in the nighttime hours, coincident with strong surface cooling. Despite this strong wind stress, the surface cooling (Q_s minima in green curve Fig. 12) appears to control the maxima in vertical mixing (blue curve in Fig. 12); that is, the maxima of RMS κ_v are consistent across the 4 days of the time series and show no discernible increase during the distinct maximum in $|\boldsymbol{\tau}^s|_{\mathrm{RMS}}$, indicating that during this period the diurnal cycle of κ_v is being primarily driven by the solar heat flux Q_s.

Time series of the RMS of submesoscale indicators (w, δ/f, ζ/f, $|\nabla_h b|$) relative to the temporal evolution of vertical mixing show responses to large $\partial\kappa_v/\partial t$ (Fig. 12, top panel). The main behavior apparent in these time series is the increase in δ/f and w RMS in response to negative $\partial\kappa_v/\partial t$. This peak in divergence RMS (i.e., peak in the strength of the secondary circulation) occurs at roughly 0900 PST each day in the time series, coincident with a sharp drop-off in κ_v. The terms ζ/f and $|\nabla_h b|$ are phase aligned and lag δ/f, w by ~2 h. The diurnal evolution of these fields is not consistent with a sequence of instantaneous TTW calculations (e.g., Figs. 11g,h). Such a diagnostic [summarized by (2)] predicts a phase alignment between κ_v and the secondary circulation (δ/f, w) for a given transverse buoyancy gradient.

Another aspect of transient evolution of fronts and filaments is a diurnal "flashing" of surface vorticity, divergence, and vertical velocity. The flashing is an increase in transverse thickness (and strength) of the latter fields illustrated with a comparison of Front1 at 0400 and 1000 PST (bottom two rows in Fig. 8). The front is (relatively) thin at 0400 PST with well-defined temperature gradient, vorticity, and divergence signals amid strong vertical mixing throughout the water column (not shown). The strength of the vertical mixing at the surface can be attributed to a uniformly negative solar heat flux ($Q_s \sim -140\,\mathrm{W\,m^{-2}}$) and a nonnegligible surface wind stress ($|\boldsymbol{\tau}^s| \sim 3\times10^{-2}\,\mathrm{N\,m^{-2}}$) oriented in a roughly cross-front direction (not shown). At 1000 PST, strong solar heat flux ($Q_s \sim 750\,\mathrm{W\,m^{-2}}$) and relative lack of wind lead to stronger stratification and less vertical mixing in the surface layer. The temperature gradient remains and is in fact somewhat stronger at 1000 (not shown). The heat flux imprint is clearly seen in the temperature map (which has been kept at the same color scale for comparison with the front at 0400 PST) with warmer temperature throughout. The lines of vorticity and divergence remain well defined and are notably wider than at 0400 PST.

The transient evolution of secondary circulations—both phasing of the secondary circulation and the

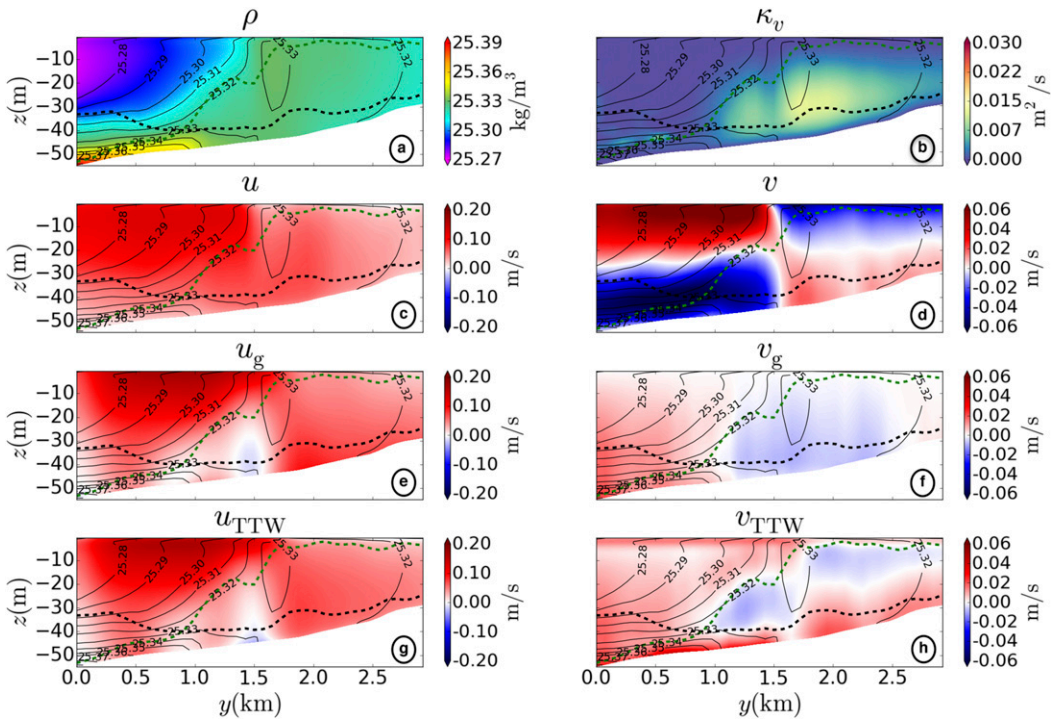

FIG. 11. As in Fig. 9, but for the Filament4 in Fig. 8. We note the name of Filament4 in reference to the overall life cycle of this density gradient structure that is analyzed in Fig. 13. Despite its frontal structure in this instantaneous 2-h average, it has a time mean over its life cycle more resembling a cold filament. Note the failure of the TTW balance to reproduce the transverse circulation v vs v_{TTW}. The failure of the TTW diagnostic is attributed to its inability to capture the full diurnal evolution of the secondary circulation as it responds to temporal changes in vertical mixing [which is weak and bottom intense in this instantaneous 2-h average, (b)].

transverse thickening/thinning of vorticity and divergence lines—is presented here as evidence of a diurnal cycle in the local circulation of fronts and filaments that has previously not been observed. Its dynamical mechanisms are investigated separately (D. Dauhajre and J. McWilliams 2017, manuscript submitted to *J. Phys. Oceanogr.*).

f. Vertical heat flux

Strong downwelling induced by the ageostrophic secondary circulations of fronts and filaments can induce vertical heat fluxes in the 3D heat balance:

$$\frac{\partial T}{\partial t} + \nabla_h \cdot \mathbf{u}_h T + \partial_z wT = \partial_z(\kappa \partial_z T). \tag{9}$$

Here, we compare the terms in (9) responsible for vertical fluxes in a shelf front or filament over 3-day periods. The heat flux caused by vertical advection J_w and by vertical mixing J_κ for a front or filament are calculated as

$$J_w = \rho_0 C_p wT', \quad J_\kappa = \rho_0 C_p \kappa_v \frac{\partial T'}{\partial z}, \tag{10}$$

where $C_p = 3985\ \mathrm{J\ kg^{-1}K^{-1}}$ is the specific heat capacity and the temperature anomaly $T' = T - \overline{T}$ is defined as the deviation from the transverse mean ($\overline{T}$) over a distance much larger than the submesoscale feature. The space–time averaging of the isolated front or filament fields results in $\overline{w} \sim 0$ and $w \sim w'$ for the heat flux calculations. We calculate a temporal average of these terms by following fronts and filaments over the course of 3 days with the same feature isolation techniques used to diagnose the secondary circulations in section 5e (cross sections rotated into a frame of reference of the front or filament at each time step). Time and longitudinal composites of fields for a front on the SPB shelf (Front2) and a cold filament on the SMB shelf (Filament4) are shown in Fig. 13 (instantaneous 2-h averages of surface fields for Front2 and Filament4 are shown in Figs. 3 and 8, respectively) The vertical heat fluxes (J_w, J_κ) in Figs. 13e, 13f, 13k, and 13l represent the net heat flux over the 3-day period. Filament4[5] and Front2

[5] We note that the density (and temperature anomaly) structure of Filament4 (Fig. 13d) exhibits asymmetry in its warm temperature anomalies surrounding the cold center. We classify this structure as a filament because it is more clearly a transverse extrema in temperature than a transverse step, as in Front2 (Fig. 13j).

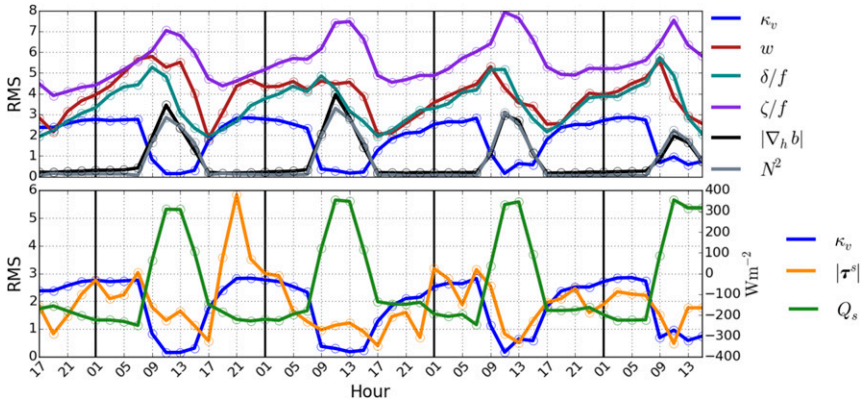

FIG. 12. A 4-day time series of spatial RMS values (starting at 1700 PST 13 Dec 2007) taken from the black dashed box in SMB shown in Fig. 2b. (top) Vertical mixing κ_v, relative vorticity ζ/f, divergence δ/f, vertical velocity w, buoyancy gradient magnitude $|\nabla_h b|$, and Brunt–Väisälä frequency squared N^2. All fields in the top panel are computed at $z = -7$ m. (bottom) Vertical mixing κ_v (at $z = -7$ m) and surface wind stress magnitude $|\boldsymbol{\tau}^s|$. Surface heat flux Q_s ($\mathrm{W\,m^{-2}}$) values are plotted corresponding to the vertical axis on the right. Dots represent 2-h-averaged individual time points. Vertical black lines separate days. Each spatial RMS for a variable is normalized by its standard deviation in time.

reside on the shelf throughout their life cycle and are chosen as the most compelling illustrative cases for this analysis (relative to the other features in Table 2). Based on similar analysis in previous work (Gula et al. 2014; McWilliams et al. 2015; McWilliams 2017), we expect a net restratifying vertical heat flux for any submesoscale secondary circulation (front or filament).

Both the front and filament are characterized by a strong time-mean negative vertical velocity [$O(10^{-2})$ $\mathrm{m\,s^{-1}}$], which peaks at middepth (Figs. 13a,g); by a nearly full mixed water column indicated by strong vertical mixing (Figs. 13b,h); by overlapping boundary layers in the time mean; and by negative temperature anomalies at the center of the cross sections (cold front and cold filament; Figs. 13d,j). The resulting vertical heat flux profiles are dominated by the positive advective heat flux J_w, which is indicative of the restratification effects of the secondary circulations. The heat fluxes caused by vertical mixing are weaker and negative. For Filament4, the advective heat flux peaks at $198\,\mathrm{W\,m^{-2}}$ at $z = -15$ m. Front2 has an even stronger advective flux of $383\,\mathrm{W\,m^{-2}}$, which peaks around middepth at $z = -20$ m. These advective fluxes are compared with vertical mixing fluxes J_κ of $-76\,\mathrm{W\,m^{-2}}$ and $-73\,\mathrm{W\,m^{-2}}$ for the front and filament, respectively.

The general picture these two cases present is that over the course of a shelf front or filament life cycle the TTW secondary circulations induce $O(100)$ $\mathrm{W\,m^{-2}}$ fluxes that act to restratify the water column and dominate over weaker heat fluxes caused by vertical mixing that opposes the restratification effects. In the context of (9), it is clear from the unequal magnitudes of J_w and J_κ that the horizontal heat flux is playing a role in this time-mean local front or filament view of the shelf. In this cross-sectional plane, the horizontal fluxes associated with the front or filament are approximately symmetric on either side of zero in a depth profile because of the symmetry of a TTW secondary circulation and because of the full-depth extent of the circulations (i.e., the shape of the secondary circulations presented in section 5e).

Breaking internal waves are usually attributed to large vertical heat fluxes on the shelf. Observations on the New Jersey shelf (Shroyer et al. 2010) show considerable instantaneous vertical heat flux because of nonlinear internal waves $J_q = \overline{\rho} C_p K_\rho T_z$, with observed J_q values as large as $790\,\mathrm{W\,m^{-2}}$. Here, $\overline{\rho}$ is an average density, $K_\rho = \Gamma\varepsilon/N^2$ is an estimated diapycnal eddy diffusivity, $\Gamma \approx 0.2$ is the turbulent mixing efficiency, ε is the local kinetic energy dissipation rate, and T_z is the vertical temperature gradient. The vertical heat flux caused by internal waves J_q acts to weaken the stratification via transport of surface heat through the pycnocline. The advective vertical heat fluxes of the fronts and filaments on the shelf J_w act in the opposite manner and restratify the water column ($w < 0$, $T' < 0$) (for a cold filament). Both processes can be responsible for substantial vertical heat fluxes on the shelf: however, internal wave fluxes are dominant in subsurface stratified conditions, while fronts and filaments typically are strongest in a more weakly stratified, near-surface layer.

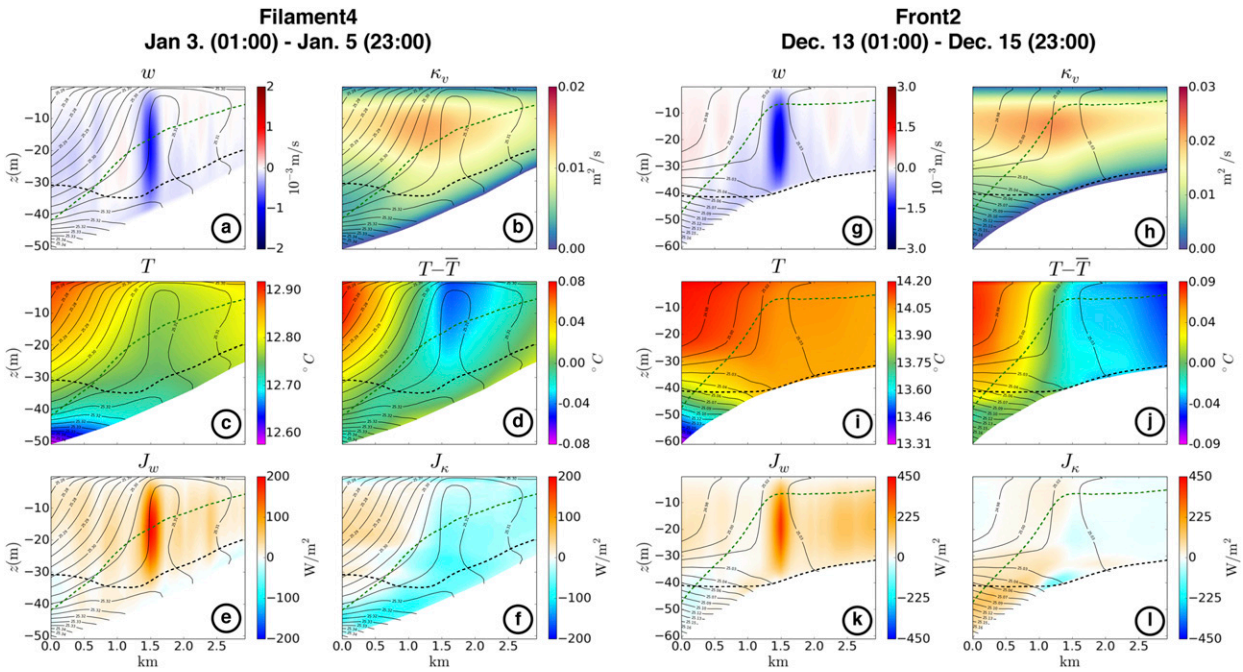

FIG. 13. Time- and longitudinal-averaged cross sections for the (left) Filament4 (0100 PST 3 Jan–2300 PST 5 Jan) and (right) Front2 (0100 PST Dec 13–2300 PST Dec 14). (a),(g) Vertical velocity, (b),(h) vertical mixing, (c),(i) temperature, (d),(j) temperature anomaly in the cross front, (e),(k) advective vertical heat flux, and (g),(l) vertical heat flux caused by turbulent vertical mixing. Black contours denote density; dashed lines denote surface (black) and bottom (green) boundary layer depths. Bottom boundary layer depth is plotted relative to the bottom (i.e., vertical extent of bottom boundary layer).

g. *Lagrangian material transport*

The relative dispersion of Lagrangian particles depends on the Eulerian velocity wavenumber spectrum, and for flows with relatively flat spectra at the submesoscales, the dispersion behavior is dominated by currents at the scale of the particle separation (LaCasce 2008; Romero et al. 2013). Furthermore, the evolution of the spatial structure of particle patches (i.e., relative dispersion) can thus be heavily controlled by the strong surface convergence associated with front and filaments on these daily time scales. The control of particle trajectories by submesoscale coherent structures has been shown for cold filaments in the Gulf Stream (Gula et al. 2014) and nearshore regions in the Santa Barbara Channel (Romero et al. 2016). The latter study put forth the hypothesis that the nearshore anisotropy in relative dispersion of particles can, in part, be due to the anisotropic spatial orientation of fronts and filaments closer to shore (i.e., the spatial geography of the submesoscale presented in section 5b). Here, we present further evidence of the ability of fronts and filaments to decrease relative dispersion and drive "self-organization" of particle patches into shapes coincident with fronts and filaments indicated by the surface convergence lines associated with secondary circulations. We also show more evidence of the diurnal cycle of secondary circulations through Lagrangian sampling of front and filament circulations.

Two types of initial particle distributions are used in this analysis. The first (front case) initializes 20 000 particles centered about a front in a circle of diameter 10 km just offshore of the SPB shelf break (Fig. 14a). The second (full domain case) initializes 93 874 particles uniformly in between the 10- and 1000-m isobaths throughout the entire domain (Fig. 14g). Both cases advect particles over the same 3-day time period. Particles are placed at the surface, neutrally buoyant, and advected only by the surface velocity field. To obtain the most accurate Lagrangian sampling of the submesoscale fields by the particles, we use 15-min snapshot ROMS output. Sensitivity tests (not shown) indicate that model output exceeding 30-min time intervals performs poorly for Lagrangian calculations in a submesoscale flow field.

Figure 14 shows the evolution of the particle positions for the front and full domain cases. In Figs. 14a–f, the particles initially distributed surrounding a front near the shelfbreak collapse onto the front 25 h after initialization because of the extreme surface convergence of the front. In Figs. 14c and 14e, the particle distribution matches the frontal structure, and material that was once near the shelf break is contained in a thin, elongated line that spans the cross-shore extent of the entire

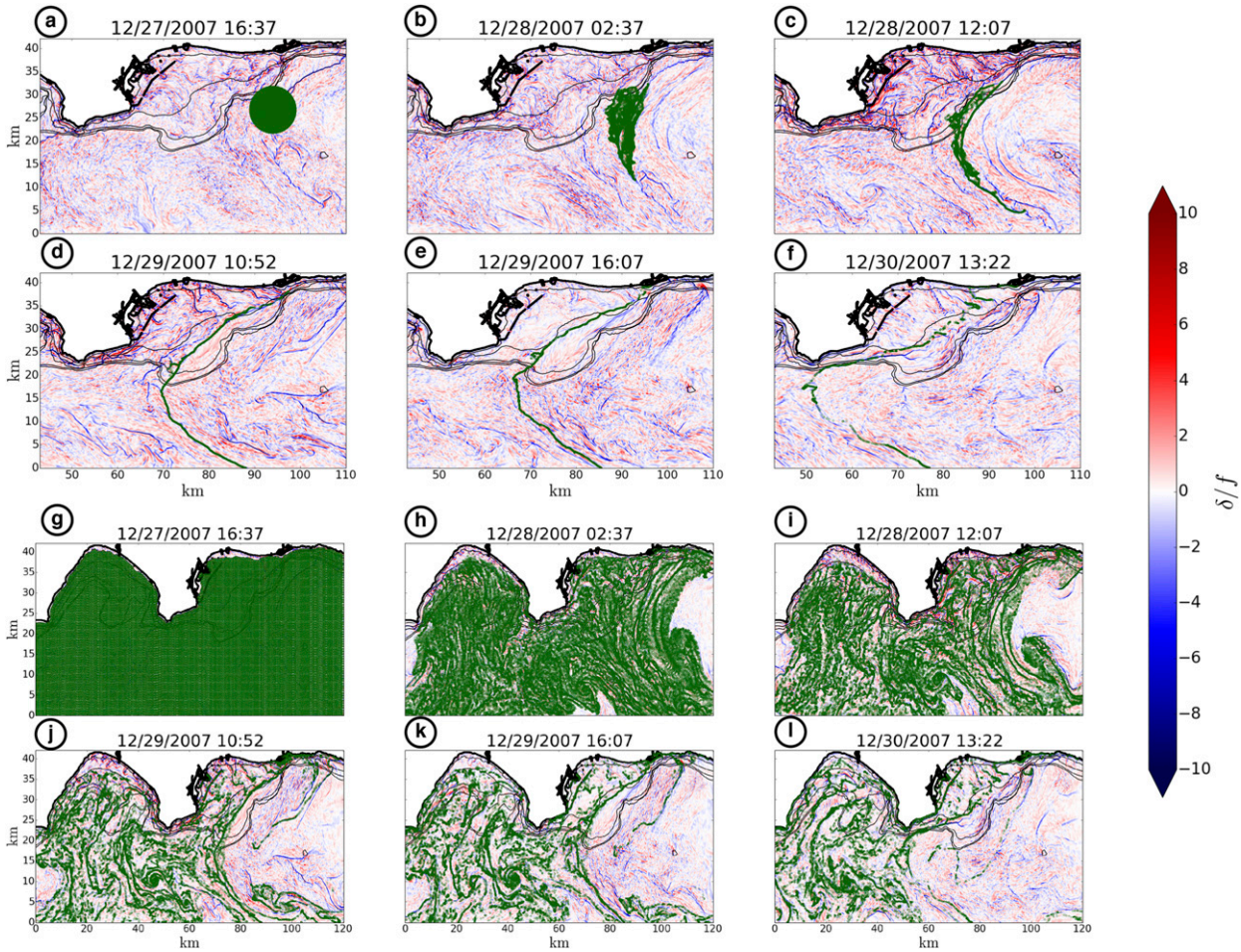

FIG. 14. Snapshots of surface divergence (colors) and Lagrangian particle evolution for particles (green circles) for two initial particle distributions: (a)–(f) front and the (g)–(l) full domain cases. Particles are neutrally buoyant, placed at the surface, and advected only by the horizontal surface velocity field. For the front case, 20 000 particles are initially distributed in a circle of diameter 10 km in (a). For the full domain case, 93 874 particles are initially distributed at all points offshore of the 10-m isobath. Time in between frames is uneven to highlight certain points in particle evolution. Note the extreme convergence and cross-shore elongation (from the shoreline to ~40 km offshore) of the particle distribution in (c)–(e), a direct consequence of the extreme surface convergence of the front.

domain. Ultimately, the front dies and surface convergence weakens, which leads to increased separation between particles (Fig. 14f). An analogous particle evolution is shown for the full domain release in Figs. 14g–l. A uniform distribution of particles ultimately ends up in surface convergence structures (lines, curves, and vortices) with some particles exiting the domain (mainly caused by a bulk advection of offshore particles through the northwestern boundary by the mean offshore current) or becoming trapped on the shoreline. These snapshots indicate the daily time scale of lateral organization of material that is induced by the submesoscale flow fields. The ultimate spatial distribution of material on these daily time scales is primarily controlled by the spatial distribution of the fronts and filaments, the advection of the fronts and filaments by larger-scale flow fields, and the location of the front or filament destruction, which can cause particle separation.

Particles trapped in convergence lines of fronts or filaments sample the temporal evolution of the front or filament circulation. Figures 15a–d show the mean and variance of particle-sampled surface divergence and relative vorticity (i.e., mean and variance over all particles of particle-coincident δ/f and ζ/f) for both the front (dark red curves) and full domain (teal curves) cases. Particles that have exited the domain or are shoreward of the 5-m isobath are not used to calculate this mean or variance. The mean vorticity and divergence show, for both cases, an initial adjustment to particles becoming

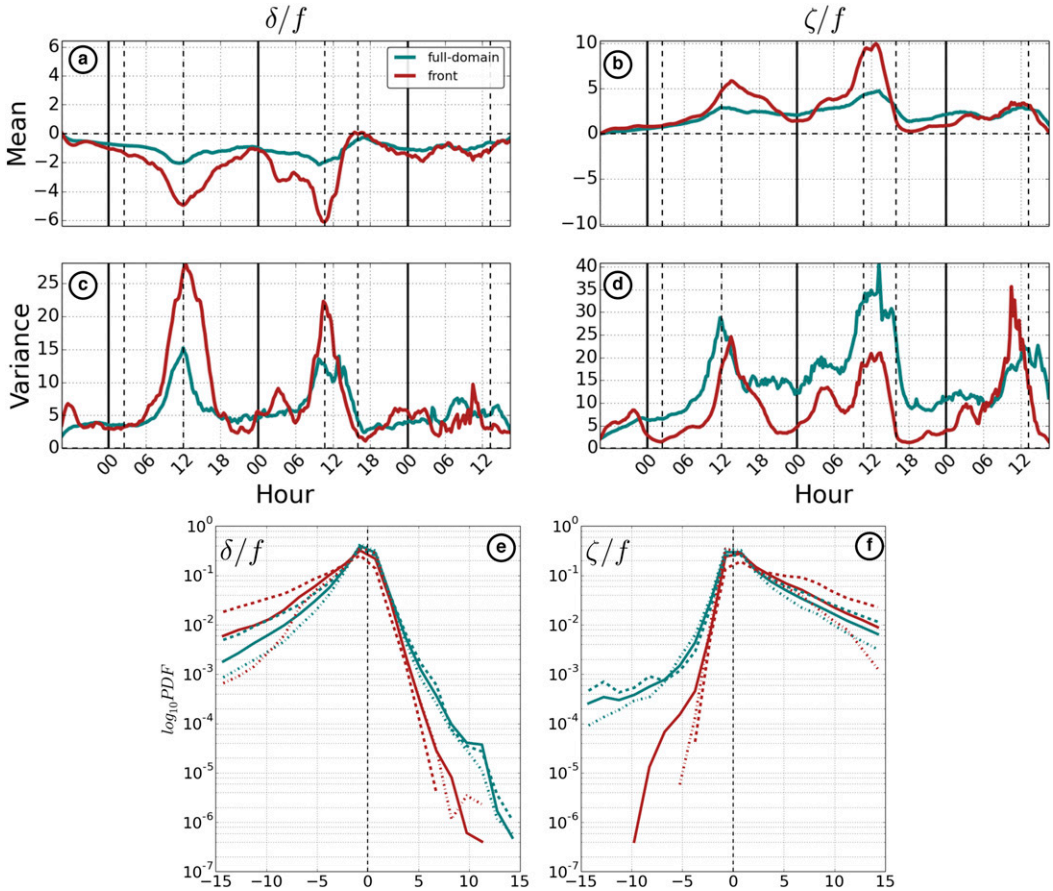

FIG. 15. Lagrangian-sampled metrics for the front (dark red) and a full domain (teal) particle distribution cases. (a)–(d) Time series (beginning at 1637 PST 27 Dec 2007) of Lagrangian-sampled (left) divergence and (right) relative vorticity; mean in (a) and (b), and variance in (c) and (d). Time series are obtained by interpolating surface fields ζ/f, δ/f to particle locations and taking the mean and variance over all particles at each time (particles that have exited the domain or are shoreward of the 5-m isobath are excluded from the mean and variance). Solid, vertical black lines indicate the start of a day and dashed vertical black lines indicate the times of the snapshots in Fig. 14. PDFs ($\log_{10}$) of Lagrangian-sampled (e) divergence and (f) vorticity. Solid curves in (e) and (f) are PDFs obtained from fields at all time points in the 3-day period [with ($N_{\text{particles}} \times 288$ time points) samples]. Dashed line PDFs represent the late-morning hour sampling (0900–1300 PST) and dashed–dotted lines represent the nighttime hour sampling (1700–2100 PST).

trapped in cyclonic, convergent structures followed by two diurnal peaks in both convergence and cyclonic vorticity. The variance of particle-sampled divergence and vorticity shows a similar evolution, with apparent diurnal peaks in δ/f and ζ/f variance for both particle distribution cases. Lagrangian analysis of ROMS solutions of the Gulf of Mexico shows a similar diurnal evolution of particle-sampled divergence and vorticity (A. Bracco and R. Barkan 2016, personal communication).

In both cases, the strongest diurnal peaks occur during the first two cycles with a less pronounced peak in particle-sampled mean convergence on the third full day. For the front case (red curves), the mean divergence shows a zero-crossing late in the day on 29 December (indicated by the second vertical dashed black line of that day). This is due to the death of the front itself; however, the particles still maintain their convergent, elongated shape at this time (Fig. 14f). The magnitude of the mean vorticity and divergence is greater for the front case because the particles are isolated over a single, very strong convergence line. The diurnal peaks in these particle-sampled metrics for divergence and vorticity indicate similar diurnal cycling of secondary circulations shown in Fig. 12. However, the specific timing of the δ/f and ζ/f peaks (1200 and 1400 PST, respectively) is different than those in Fig. 12 (0900 and 1100 PST). Reasons for this difference in phasing [e.g., variability in $\kappa_v(t)$ temporal structure] will be

investigated in D. Dauhajre and J. McWilliams (2017, manuscript submitted to *J. Phys. Oceanogr.*).

PDFs of particle-sampled divergence and vorticity (Figs. 15e,f) show that particles tend to be trapped by submesoscale coherent structures on the whole. For both releases, the PDFs are skewed toward negative divergence and cyclonic vorticity (solid lines). This skewness is more exaggerated when the sampling points are taken to be only in the late morning (dashed lines), defined as 0900–1300 PST, and less exaggerated when sampling points are taken to be in the night (dashed–dotted lines), defined as 1700–2100 PST. Again, this metric indicates that surface material, on daily time scales, is trapped in submesoscale structures of strong surface convergence and strong cyclonic vorticity. The strength of this convergence and vorticity exhibits a diurnal cycle that peaks in the late morning, signifying a transient response of secondary circulation to $\partial\kappa_v/\partial t \neq 0$. This diurnal signal is captured in the full domain case (Fig. 15, teal curves) where particles are sampling flow fields on and off the shelf; the diurnal evolution of vorticity and divergence is likely to be similar between shelf and open-ocean submesoscale currents.

6. Summary, conclusions, and prospects

The existence of submesoscale variability (in the form of fronts, filaments, and vortices) on the shelf is shown through a numerical simulation of the Southern California Bight with horizontal resolution $\Delta x = 75\,\mathrm{m}$. Fronts and filaments defined by large horizontal buoyancy gradients coincident with strong surface convergence and cyclonic vorticity are ubiquitous on the shelf with lifetimes on the order of days. No paradigms previously used to describe shelf circulation predict the existence of these phenomena. These spontaneously formed and short-lived submesoscale density gradients differ in dynamical classification ($\mathrm{Ro} \gg 1$) and evolution from the persistent and geographically constrained shelfbreak and tidal mixing fronts that are commonly found on some continental shelves. Submesoscale currents on the shelf are frequently in contact with the seafloor; the shallow depth of the shelf is the primary source for differences in the phenomenology of open-ocean and shallow-water submesoscale dynamics. This study attempts to characterize the submesoscale regime on the shelf and, as such, raises a number of questions for further investigation.

Colder atmospheric temperatures along with more frequent storms lead to a less stratified shelf relative to other times of year. On some shelves with very strong storms or cooling the winter stratification disappears entirely (e.g., off New England), unlike in the SCB where a pycnocline is always present over most of the shelf. Callies et al. (2015) observe a seasonal cycle in submesoscale turbulence in the Gulf Stream, with stronger submesoscale activity in the winter months because of decreased stratification and deeper surface mixed layers. It is possible that the low stratification associated with the winter–spring months of the L3 solution may lead to an overrepresentation of the submesoscale activity relative to summer months when stratification is higher. However, further investigation into the seasonality of shallow-water submesoscale variability is warranted given the BBL whose vertical mixing (and thus TTW secondary circulations) can potentially induce frontogenesis in the absence of surface cooling.

Generally, there is stronger submesoscale variance (indicated by ζ/f, δ/f variance) on the shelf relative to offshore. The shelf submesoscale variance is diminished inshore of ~10-m isobath in our simulation. However, this result should be readdressed with submesoscale-resolving simulations that include an active surfzone. The coastal submesoscale geography is influenced by the local bathymetry and shape of the coastline. Shallow-water [$h \sim O(10)$ m] fronts and filaments show a preference for longitudinal alignment parallel to isobaths. This preference is less pronounced as depth increases with essentially isotropic orientations offshore. Headlands are sites of extreme vorticity variance and can act as the source point for submesoscale structure generation in a bay.

The formation mechanisms responsible for creating submesoscale gradients on the shelf are distinct from the mechanisms responsible for creating tidal mixing and shelfbreak fronts. Similar to their open-ocean analogs, horizontal advection is the dominant process responsible for increasing and elongating submesoscale density and velocity gradients on the shelf. However, local bathymetry can greatly influence formation. We present a case of a headland wake as an example of these two controls: coastline influenced cyclonic vorticity generation combined with frontogenesis dominated by horizontal advection. The fraction of coastal submesoscale activity caused by shelf-specific controls on formation (creation of straining flows by topographic steering and frontogenesis from headland wake formation) or more general mechanisms that are perennially present in the open-ocean regime (frontogenesis by mesoscale straining flows or secondary circulations in a turbulent boundary layer and mixed layer instabilities) remains to be quantified.

The transverse structure of shelf fronts and filaments exhibit less transverse symmetry compared to their offshore counterparts. This asymmetry is manifested in isopycnal and vertical mixing structures (e.g., Fig. 9). The most

likely control of the asymmetry is the interaction of full-depth boundary layers on a slope, which generally causes a decrease in vertical mixing strength closer to shore. Offshore SBLs have no such interaction with the bottom.

The quasi-steady TTW diagnostic balance matches shelf front and filament secondary circulations at times of strong vertical mixing in the SBL. However, sometimes there is a clear diurnal evolution of the secondary circulation that is not consistent with a steady model. This diurnal evolution is characterized by a transient response of front and filament circulations to abrupt changes in the vertical mixing. The response primarily appears as a phase lag between peaks in mixing and divergence. The mechanism(s) controlling the diurnal evolution of secondary circulations is being investigated separately (D. Dauhajre and J. McWilliams 2017, manuscript submitted to *J. Phys. Oceanogr.*).

Over a submesoscale life cycle, the strong downwelling associated with the secondary circulation can be responsible for vertical heat fluxes on the order of $100\,\mathrm{W\,m^{-2}}$ over the area occupied by the feature. These fluxes act to restratify the water column and are comparable in magnitude to observed vertical heat fluxes associated with breaking internal waves on the New Jersey shelf that act to mix in the pycnocline. The local heat flux calculations presented in this study do not constitute a full analysis of the statistically dominant terms in the heat balance on the shelf. Rather, we have presented the general question of vertical heat fluxes and stratification on the shelf in relation to internal wave and submesoscale TTW fluxes. To what degree do submesoscale TTW fluxes set the stratification on the shelf?

The prevalence of submesoscale coherent structures on the shelf raises many obvious questions regarding their role in controlling the fate of material in the nearshore. On daily time scales, material on the shelf is preferentially trapped into surface convergence lines associated with fronts and filaments. Submesoscale currents should certainly be added to the inventory of shelf circulations responsible for lateral fluxes on the shelf (e.g., internal waves, cross-shelf winds). Lagrangian particles, used to sample the velocity gradients, provide alternate evidence of the diurnal cycle of front and filament secondary circulations; this evidence is derived from particles on and off the shelf and suggests this diurnal evolution is universal to fronts and filaments regardless of total depth. The strong downwelling associated with the convergence can drive this material into the interior once it is laterally advected into the center of a front or filament.

Explicit diagnostics of submesoscale control on material dispersion has applications in ecology (e.g., larval dispersal) as well as coastal management (e.g., urban runoff and pollution). Using submesoscale-resolving ROMS solutions of the SCB shelf, Uchiyama et al. (2014) and Romero et al. (2013) show that the submesoscale regime is more responsible for the dispersion of material on the shelf than the mean currents and tides. What these studies do not diagnose, however, is the role of submesoscale variability in controlling regional connectivity (Mitari et al. 2009). High-resolution simulations of the coastal ocean provide an updated tool [relative to the $\Delta x = 1\,\mathrm{km}$ solutions of Mitari et al. (2009)] to inform ecological frameworks (e.g., Castorani et al. 2015) that rely on physical parameters such as oceanographic connectivity between coastal sites. Further, the general role that the nearshore submesoscale regime plays in controlling coastal connectivity patterns remains unknown and needs to be explored. Is submesoscale resolution needed to accurately assess and/or predict the fate of material in the nearshore?

An obvious route of discovery (and validation) lies in the development of coastal observational platforms capable of better resolving submesoscale processes. Nearshore observational platforms (fast, maneuverable boats, gliders, and/or planes) seeking to "hunt" short-lived shelf fronts and filaments can maximize their strike rate by looking for temperature gradient signals across isobaths and potentially near headlands. Along with general field campaigns aimed at gaining a bulk understanding of the submesoscale regime on the shelf, we specifically encourage the pursuit for diurnal sampling of secondary circulations. To our knowledge, the metrics shown in sections 5e(ii) and 5g represent first realizations (numerical or real world) of diurnal variability of front and filament secondary circulation.

Acknowledgments. We thank Jonathan Gula for initial guidance on analysis techniques. This research is supported by NSF OCE-1355970 and ONR N00014-14-1-0626 at UCLA, NSF LTER at UCSB, and NSF XSEDE computing.

REFERENCES

Austin, J., and S. Lentz, 2002: The inner shelf response to wind-driven upwelling and downwelling. *J. Phys. Oceanogr.*, **32**, 2171–2193, https://doi.org/10.1175/1520-0485(2002)032<2171:TISRTW>2.0.CO;2.

Barkan, R., K. Winters, and S. L. Smith, 2015: Energy cascades and loss of balance in a reentrant channel forced by wind stress and buoyancy fluxes. *J. Phys. Oceanogr.*, **45**, 272–293, https://doi.org/10.1175/JPO-D-14-0068.1.

Bassin, C., and L. Washburn, 2005: Sub-mesoscale coastal eddies observed by high frequency radar: A new mechanism for delivering nutrients to kelp forests in the Southern California Bight. *Geophys. Res. Lett.*, **32**, L12604, https://doi.org/10.1029/2005GL023017.

Benthuysen, J., L. Thomas, and S. Lentz, 2015: Rapid generation of upwelling at a shelf break caused by buoyancy shutdown. *J. Phys. Oceanogr.*, **45**, 294–312, https://doi.org/10.1175/JPO-D-14-0104.1.

Boccaletti, G., R. Ferrari, and B. Fox-Kemper, 2007: Mixed layer instabilities and restratification. *J. Phys. Oceanogr.*, **37**, 2228–2250, https://doi.org/10.1175/JPO3101.1.

Bracco, A., J. Choi, K. Joshi, H. Luo, and J. McWilliams, 2016: Submesoscale currents in the northern Gulf of Mexico: Deep phenomena and dispersion over the continental slope. *Ocean Modell.*, **101**, 43–58, https://doi.org/10.1016/j.ocemod.2016.03.002.

Buijsman, M., Y. Uchiyama, J. McWilliams, and C. Hill-Lindsay, 2012: Modeling semidiurnal internal tide variability in the Southern California Bight. *J. Phys. Oceanogr.*, **42**, 62–77, https://doi.org/10.1175/2011JPO4597.1.

Callies, J., R. Ferrari, J. M. Klymax, and J. Gula, 2015: Seasonality in submesoscale turbulence. *Nat. Commun.*, **6**, 6862–6870, https://doi.org/10.1038/ncomms7862.

——, G. Flierl, R. Ferrari, and B. Fox-Kemper, 2016: The role of mixed-layer instabilities in submesoscale turbulence. *J. Fluid Mech.*, **788**, 5–41, https://doi.org/10.1017/jfm.2015.700.

Capet, X., E. Campos, and A. Paiva, 2008a: Submesoscale activity over the Argentinian shelf. *Geophys. Res. Lett.*, **35**, L15605, https://doi.org/10.1029/2008GL034736.

——, J. McWilliams, M. Molemaker, and A. Shchepetkin, 2008b: Mesoscale to submesoscale transition in the California Current System. Part I: Flow structure, eddy flux, and observational tests. *J. Phys. Oceanogr.*, **38**, 29–43, https://doi.org/10.1175/2007JPO3671.1.

——, ——, ——, and ——, 2008c: Mesoscale to submesoscale transition in the California Current System. Part II: Frontal processes. *J. Phys. Oceanogr.*, **38**, 44–64, https://doi.org/10.1175/2007JPO3672.1.

——, ——, ——, and ——, 2008d: Mesoscale to submesoscale transition in the California Current System. Part III: Energy balance and flux. *J. Phys. Oceanogr.*, **38**, 2256–2269, https://doi.org/10.1175/2008JPO3810.1.

Castorani, M. C., D. Reed, F. Alberto, T. Bell, R. Simons, K. Cavanaugh, D. Siegel, and P. Raimondi, 2015: Connectivity structures local population dynamics: A long-term empirical test in a large metapopulation system. *Ecology*, **96**, 3141–3152, https://doi.org/10.1890/15-0283.1.

Chapman, D., 1986: A simple model of the formation and maintenance of the shelf/slope front in the Middle Atlantic Bight. *J. Phys. Oceanogr.*, **16**, 1273–1279, https://doi.org/10.1175/1520-0485(1986)016<1273:ASMOTF>2.0.CO;2.

——, 1987: Application of wind-forced, long, coastal-trapped wave theory along the California coast. *J. Geophys. Res.*, **92**, 1798–1816, https://doi.org/10.1029/JC092iC02p01798.

——, 2000: Boundary layer control of buoyant coastal currents and the establishment of a shelfbreak front. *J. Phys. Oceanogr.*, **30**, 2941–2955, https://doi.org/10.1175/1520-0485(2001)031<2941:BLCOBC>2.0.CO;2.

——, and R. Beardsley, 1989: On the origin of shelf water in the Middle Atlantic Bight. *J. Phys. Oceanogr.*, **19**, 384–391, https://doi.org/10.1175/1520-0485(1989)019<0384:OTOOSW>2.0.CO;2.

——, and S. Lentz, 1994: Trapping of a coastal density front by the bottom boundary layer. *J. Phys. Oceanogr.*, **24**, 1464–1479, https://doi.org/10.1175/1520-0485(1994)024<1464:TOACDF>2.0.CO;2.

——, and ——, 2005: Acceleration of a stratified current over a sloping bottom, driven by an alongshelf pressure gradient. *J. Phys. Oceanogr.*, **35**, 1305–1317, https://doi.org/10.1175/JPO2744.1.

Chen, C., R. Beardsley, P. Franks, and J. Van Keuren, 2003: Influence of diurnal heating on stratification and residual circulation of Georges Bank. *J. Geophys. Res.*, **108**, 8008, https://doi.org/10.1029/2001JC001245.

Chen, K., and R. He, 2010: Numerical investigation of the Middle Atlantic Bight shelfbreak frontal circulation using a high-resolution ocean hindcast model. *J. Phys. Oceanogr.*, **40**, 949–964, https://doi.org/10.1175/2009JPO4262.1.

Cudaback, C., and L. Washburn, 2005: Subtidal inner-shelf circulation near Point Conception, California. *J. Geophys. Res.*, **110**, C10007, https://doi.org/10.1029/2004JC002608.

Dale, A., D. Ullman, J. Barth, and D. Hebert, 2003: The front on the northern flank of Georges Bank in spring: 1. Tidal and subtidal variability. *J. Geophys. Res.*, **108**, 8009, https://doi.org/10.1029/2002JC001327.

D'Asaro, E., C. Lee, L. Rainville, R. Harcourt, and L. Thomas, 2011: Enhanced turbulence and energy dissipation at ocean fronts. *Science*, **332**, 318–322, https://doi.org/10.1126/science.1201515.

Dever, E., 1997: Wind-forced cross-shelf circulation on the Northern California shelf. *J. Phys. Oceanogr.*, **27**, 1566–1580, https://doi.org/10.1175/1520-0485(1997)027<1566:WFCSCO>2.0.CO;2.

DiGiacomo, P., and B. Holt, 2001: Satellite observations of small coastal ocean eddies in the Southern California Bight. *J. Geophys. Res.*, **106**, 22 521–22 543, https://doi.org/10.1029/2000JC000728.

Durski, S., S. Glenn, and D. Haidvogel, 2004: Vertical mixing schemes in the coastal ocean: Comparison of the level 2.5 Mellor-Yamada scheme with an enhanced version of the K profile parameterization. *Geophys. Res. Lett.*, **109**, C01015, https://doi.org/10.1029/2002JC001702.

Egbert, G., A. Bennet, and M. Foreman, 1994: TOPEX/Poseidon tides estimated using a global inverse model. *J. Geophys. Res.*, **99**, 24 821–24 852, https://doi.org/10.1029/94JC01894.

Feddersen, F., R. Guza, S. Elgar, and T. Herbers, 1998: Alongshore momentum balances in the nearshore. *J. Geophys. Res.*, **103**, 15 667–15 676, https://doi.org/10.1029/98JC01270.

Federiuk, J., and J. Allen, 1996: Model studies of near-inertial waves in flow over the Oregon continental shelf. *J. Phys. Oceanogr.*, **26**, 2053–2075, https://doi.org/10.1175/1520-0485(1996)026<2053:MSONIW>2.0.CO;2.

Furukawa, K., and E. Wolanski, 1998: Shallow-water frictional effects in island wakes. *Estuarine Coastal Shelf Sci.*, **46**, 599–608, https://doi.org/10.1006/ecss.1997.0301.

Ganju, N., S. Lentz, A. Kirincich, and J. Farrar, 2011: Complex mean circulation over the inner shelf south of Martha's Vineyard revealed by observations and a high-resolution model. *J. Geophys. Res.*, **116**, C10036, https://doi.org/10.1029/2011JC007035.

Garrett, C., and J. Loder, 1981: Dynamical aspects of shallow sea fronts. *Philos. Trans. Roy. Soc. London*, **B302**, 563–581, https://doi.org/10.1098/rsta.1981.0183.

Geyer, W., and R. Signell, 1990: Measurements of tidal flow around a headland with a shipboard acoustic Doppler current profiler. *J. Geophys. Res.*, **95**, 3189–3197, https://doi.org/10.1029/JC095iC03p03189.

Gula, J., M. Molemaker, and J. McWilliams, 2014: Submesoscale cold filaments in the Gulf Stream. *J. Phys. Oceanogr.*, **44**, 2617–2643, https://doi.org/10.1175/JPO-D-14-0029.1.

Hickey, B., E. Dobbins, and S. Allen, 2003: Local and remote forcing of currents and temperature in the central Southern California Bight. *J. Geophys. Res.*, **108**, 3081, https://doi.org/10.1029/2000JC000313.

Hill, A., and Coauthors, 1993: Dynamics of tidal mixing fronts in the North Sea. *Philos. Trans. Roy. Soc. London*, **B343**, 431–446, https://doi.org/10.1098/rsta.1993.0057.

Hoskins, B., 1982: The mathematical theory of frontogenesis. *Annu. Rev. Fluid Mech.*, **14**, 131–151, https://doi.org/10.1146/annurev.fl.14.010182.001023.

Kim, S., and Coauthors, 2013: Poleward propagating subinertial alongshore surface currents off the U.S. West Coast. *J. Geophys. Res. Oceans*, **118**, 6791–6806, https://doi.org/10.1002/jgrc.20400.

Kirincich, A., 2016: The occurrence, drivers, and implications of submesoscale eddies on Martha's Vineyard inner shelf. *J. Phys. Oceanogr.*, **46**, 2645–2662, https://doi.org/10.1175/JPO-D-15-0191.1.

——, S. Lentz, and J. Barth, 2009: Wave-driven inner-shelf motions on the Oregon coast. *J. Phys. Oceanogr.*, **39**, 2942–2956, https://doi.org/10.1175/2009JPO4041.1.

Kumar, N., F. Feddersen, Y. Uchiyama, J. McWilliams, and W. O'Reilly, 2015: Midshelf to surfzone coupled ROMS–SWAN model data comparison of waves, currents, and temperature: Diagnosis of subtidal forcings and response. *J. Phys. Oceanogr.*, **45**, 1464–1490, https://doi.org/10.1175/JPO-D-14-0151.1.

——, ——, S. Suanda, Y. Uchiyama, and J. McWilliams, 2016: Mid- to inner-shelf coupled ROMS–SWAN model–data comparison of currents and temperature: Diurnal and semidiurnal variability. *J. Phys. Oceanogr.*, **46**, 841–862, https://doi.org/10.1175/JPO-D-15-0103.1.

LaCasce, J., 2008: Statistics from Lagrangian observations. *Prog. Oceanogr.*, **77**, 1–29, https://doi.org/10.1016/j.pocean.2008.02.002.

Large, W., J. McWilliams, and S. Doney, 1994: Oceanic vertical mixing: A review and a model with a nonlocal boundary layer parameterization. *Rev. Geophys.*, **32**, 363–403, https://doi.org/10.1029/94RG01872.

Lemarie, F., J. Kurian, A. Shchepetkin, M. Molemaker, F. Colas, and J. McWilliams, 2012: Are there inescapable issues prohibiting the use of terrain-following coordinates in climate models? *Ocean Modell.*, **42**, 57–79, https://doi.org/10.1016/j.ocemod.2011.11.007.

Lentz, S., and C. Winant, 1986: Subinertial currents on the Southern California shelf. *J. Phys. Oceanogr.*, **16**, 1737–1750, https://doi.org/10.1175/1520-0485(1986)016<1737:SCOTSC>2.0.CO;2.

——, and D. Chapman, 2004: The importance of nonlinear cross-shelf momentum flux during wind-driven coastal upwelling. *J. Phys. Oceanogr.*, **34**, 2444–2457, https://doi.org/10.1175/JPO2644.1.

——, and M. Fewings, 2012: The wind- and wave-driven inner-shelf circulation. *Annu. Rev. Mar. Sci.*, **4**, 317–343, https://doi.org/10.1146/annurev-marine-120709-142745.

Lerczak, J., M. Hendershott, and C. Winant, 2001: Observations and modeling of coastal internal waves driven by a diurnal sea breeze. *J. Geophys. Res.*, **106**, 19 715–19 729, https://doi.org/10.1029/2001JC000811.

——, C. Winant, and M. Hendershott, 2003: Observations of the semidiurnal internal tide on the Southern California slope and shelf. *J. Geophys. Res.*, **108**, 3068, https://doi.org/10.1029/2001JC001128.

Levy, M., R. Ferrari, P. Franks, A. Martin, and P. Riviere, 2012: Bringing physics to life at the submesoscale. *Geophys. Res. Lett.*, **39**, L14602, doi:10.1029/2012GL052756.

Linder, C., and G. Gawarkiewicz, 1998: A climatology of the shelfbreak front in the Middle Atlantic Bight. *J. Geophys. Res.*, **103**, 18 405–18 423, https://doi.org/10.1029/98JC01438.

Loder, J., K. Drinkwater, N. Oakey, and E. Horne, 1993: Understanding the North Sea system—Circulation, hydrographic structure and mixing at tidal fronts: The view from Georges Bank. *Philos. Trans. Roy. Soc. London*, **B343**, 447–460, https://doi.org/10.1098/rsta.1993.0058.

Maddock, L., and R. Pingree, 1978: Numerical simulation of the Portland tidal eddies. *Estuarine Coastal Mar. Sci.*, **6**, 353–363, https://doi.org/10.1016/0302-3524(78)90127-5.

Mahadevan, A., 2016: The impact of submesoscale physics on primary productivity of plankton. *Annu. Rev. Mar. Sci.*, **8**, 161–184, https://doi.org/10.1146/annurev-marine-010814-015912.

——, and A. Tandon, 2006a: An analysis of mechanisms for submesoscale vertical motion at ocean fronts. *Ocean Modell.*, **14**, 241–256, https://doi.org/10.1016/j.ocemod.2006.05.006.

——, and ——, 2006b: Modeling vertical motion at ocean fronts: Are nonhydrostatic effects relevant at submesoscales? *Ocean Modell.*, **14**, 222–240, https://doi.org/10.1016/j.ocemod.2006.05.005.

Mason, E., J. Molemaker, A. Shchepetkin, F. Colas, J. McWilliams, and P. Sangra, 2010: Procedures for offline grid nesting in regional ocean models. *Ocean Modell.*, **35**, 1–15, https://doi.org/10.1016/j.ocemod.2010.05.007.

McWilliams, J., 2016: Submesoscale currents in the ocean. *Proc. Roy. Soc.*, **A472**, 20160117, https://doi.org/10.1098/rspa.2016.0117.

——, 2017: Submesoscale surface fronts and filaments: Secondary circulation, buoyancy flux, and frontogenesis. *J. Fluid Mech.*, **823**, 391–432, https://doi.org/10.1017/jfm.2017.294.

——, F. Colas, and J. Molemaker, 2009a: Cold filamentary intensification and oceanic surface convergence lines. *Geophys. Res. Lett.*, **36**, L18602, https://doi.org/10.1029/2009GL039402.

——, E. Huckle, and A. Shchepetkin, 2009b: Buoyancy effects in a stratified Ekman layer. *J. Phys. Oceanogr.*, **39**, 2581–2599, https://doi.org/10.1175/2009JPO4130.1.

——, M. Molemaker, and E. Olafsdottir, 2009c: Linear fluctuation growth during frontogenesis. *J. Phys. Oceanogr.*, **39**, 3111–3129, https://doi.org/10.1175/2009JPO4186.1.

——, J. Gula, J. Molemaker, L. Renault, and A. Shchepetkin, 2015: Filament frontogenesis by boundary layer turbulence. *J. Phys. Oceanogr.*, **45**, 1988–2005, https://doi.org/10.1175/JPO-D-14-0211.1.

Michalakes, J., J. Dudhia, D. Gill, J. Klemp, and W. Skamarock, 1998: Design of a next-generation regional weather research and forecast model. *Proc. Eighth Workshop on the Use of Parallel Processors in Meteorology*, Reading, United Kingdom, European Centre for Medium-Range Weather Forecasts, 117–124.

Mitari, S., D. Siegel, J. Watson, C. Dong, and J. McWilliams, 2009: Quantifying connectivity in the coastal ocean with application to the Southern California Bight. *J. Geophys. Res.*, **114**, C10026, https://doi.org/10.1029/2008JC005166.

Molemaker, M., J. McWilliams, and W. Dewar, 2015: Submesoscale instability and generation of mesoscale anticyclones near a separation of the California Undercurrent. *J. Phys. Oceanogr.*, **45**, 613–629, https://doi.org/10.1175/JPO-D-13-0225.1.

Munk, W., L. Armi, K. Fischer, and F. Zachariasen, 2000: Spirals on the sea. *Proc. Roy. Soc. London*, **456**, 1217–1280, https://doi.org/10.1098/rspa.2000.0560.

Nagai, T., A. Tandon, and D. Rudnick, 2006: Two-dimensional ageostrophic secondary circulations at ocean fronts due to vertical mixing and large-scale deformation. *J. Geophys. Res.*, **111**, C09038, https://doi.org/10.1029/2005JC002964.

Nam, S., and U. Send, 2013: Resonant diurnal oscillations and mean alongshore flows driven by sea/land breeze forcing in the coastal Southern California Bight. *J. Phys. Oceanogr.*, **43**, 616–630, https://doi.org/10.1175/JPO-D-11-0148.1.

Noble, M., B. Jones, P. Hamilton, J. Xu, G. Robertson, L. Rosenfeld, and J. Largier, 2009: Cross-shelf transport into nearshore waters due to shoaling internal tides in San Pedro Bay, CA. *Cont. Shelf Res.*, **29**, 1768–1785, https://doi.org/10.1016/j.csr.2009.04.008.

Robinson, I., 1981: Tidal vorticity and residual circulation. *Deep-Sea Res.*, **28**, 195–212, https://doi.org/10.1016/0198-0149(81)90062-5.

Romero, L., Y. Uchiyama, J. C. Ohlmann, J. C. McWilliams, and D. A. Siegel, 2013: Simulations of nearshore particle-pair dispersion in Southern California. *J. Phys. Oceanogr.*, **43**, 1862–1879, https://doi.org/10.1175/JPO-D-13-011.1.

——, D. Siegel, J. McWilliams, Y. Uchiyama, and C. Jones, 2016: Characterizing storm water dispersion and dilution from small coastal streams. *J. Geophys. Res. Oceans*, **121**, 3926–3943, https://doi.org/10.1002/2015JC011323.

Shakespeare, C., and J. Taylor, 2013: A generalized mathematical model of geostrophic adjustment and frontogenesis: Uniform potential vorticity. *J. Fluid Mech.*, **736**, 366–413, https://doi.org/10.1017/jfm.2013.526.

Shchepetkin, A., and J. McWilliams, 2005: The Regional Oceanic Modeling System (ROMS): A split-explicit, free-surface, topography-following-coordinate ocean model. *Ocean Modell.*, **9**, 347–404, https://doi.org/10.1016/j.ocemod.2004.08.002.

Shcherbina, A., E. D'Asara, C. Lee, J. Klymak, M. Molemaker, and J. McWilliams, 2013: Statistics of vertical vorticity, divergence, and strain in a developed submesoscale turbulence field. *Geophys. Res. Lett.*, **40**, 4706–4711, https://doi.org/10.1002/grl.50919.

Shroyer, E., J. Moum, and J. Nash, 2010: Vertical heat flux and lateral mass transport in nonlinear internal waves. *Geophys. Res. Lett.*, **37**, L08601, https://doi.org/10.1029/2010GL042715.

Simpson, J., 1981: The shelf-sea fronts: Implications of their existence and behavior. *Philos. Trans. Roy. Soc. London*, **B302**, 531–546, https://doi.org/10.1098/rsta.1981.0181.

——, and J. Hunter, 1974: Fronts in the Irish Sea. *Nat. Commun.*, **250**, 404–406, https://doi.org/10.1038/250404a0.

Tilburg, C., 2003: Across-shelf transport on a continental shelf: Do across-shelf winds matter? *J. Phys. Oceanogr.*, **33**, 2675–2688, https://doi.org/10.1175/1520-0485(2003)033<2675:ATOACS>2.0.CO;2.

Tomczak, M., 1988: Island wakes in deep and shallow water. *J. Geophys. Res.*, **93**, 5153–5154, https://doi.org/10.1029/JC093iC05p05153.

Uchiyama, Y., E. Idica, J. McWilliams, and K. Stolzenbach, 2014: Wastewater effluent dispersal in Southern California bays. *Cont. Shelf Res.*, **76**, 36–52, https://doi.org/10.1016/j.csr.2014.01.002.

Ullman, D., A. Dale, D. Hebert, and J. Barth, 2003: The front on the northern flank of Georges Bank in spring: 2. Cross-frontal fluxes and mixing. *J. Geophys. Res.*, **108**, 8010, https://doi.org/10.1029/2002JC001328.

Wenegrat, J., and M. McPhaden, 2016: Wind, waves and fronts: Frictional effects in a generalized Ekman model. *J. Phys. Oceanogr.*, **46**, 371–394, https://doi.org/10.1175/JPO-D-15-0162.1.

Wolanski, E., J. Imberger, and M. Heron, 1984: Island wakes in shallow coastal waters. *J. Geophys. Res.*, **89**, 10 533–10 569, https://doi.org/10.1029/JC089iC06p10553.

Zhang, W., and G. Gawarkiewicz, 2015: Length scale of the finite-amplitude meanders of shelfbreak fronts. *J. Phys. Oceanogr.*, **45**, 2598–2620, https://doi.org/10.1175/JPO-D-14-0249.1.